Relationships between resting conductances, excitability, and t-system ionic homeostasis in skeletal muscle

James A. Fraser,[1] Christopher L.-H. Huang,[1] and Thomas H. Pedersen[1,2]

[1]Physiological Laboratory, University of Cambridge, Cambridge CB2 3EG, England, UK
[2]Department of Physiology and Biophysics, Aarhus University, 8000 Aarhus, Denmark

Activation of skeletal muscle fibers requires rapid sarcolemmal action potential (AP) conduction to ensure uniform excitation along the fiber length, as well as successful tubular excitation to initiate excitation–contraction coupling. In our companion paper in this issue, Pedersen et al. (2011. *J. Gen. Physiol.* doi:10.1085/jgp.201010510) quantify, for subthreshold stimuli, the influence upon both surface conduction velocity and tubular (t)-system excitation of the large changes in resting membrane conductance (G_M) that occur during repetitive AP firing. The present work extends the analysis by developing a multi-compartment modification of the charge–difference model of Fraser and Huang to provide a quantitative description of the conduction velocity of actively propagated APs; the influence of voltage-gated ion channels within the t-system; the influence of t-system APs on ionic homeostasis within the t-system; the influence of t-system ion concentration changes on membrane potentials; and the influence of Phase I and Phase II G_M changes on these relationships. Passive conduction properties of the novel model agreed with established linear circuit analysis and previous experimental results, while key simulations of AP firing were tested against focused experimental microelectrode measurements of membrane potential. This study thereby first quantified the effects of the t-system luminal resistance and voltage-gated Na^+ channel density on surface AP propagation and the resultant electrical response of the t-system. Second, it demonstrated the influence of G_M changes during repetitive AP firing upon surface and t-system excitability. Third, it showed that significant K^+ accumulation occurs within the t-system during repetitive AP firing and produces a baseline depolarization of the surface membrane potential. Finally, it indicated that G_M changes during repetitive AP firing significantly influence both t-system K^+ accumulation and its influence on the resting membrane potential. Thus, the present study emerges with a quantitative description of the changes in membrane potential, excitability, and t-system ionic homeostasis that occur during repetitive AP firing in skeletal muscle.

INTRODUCTION

Recent studies have demonstrated that the resting membrane conductance (G_M) of skeletal muscle is highly regulated during repetitive firing of short trains of action potentials (APs) that replicate excitation patterns occurring during activity in skeletal muscle (Pedersen et al., 2009a,b). In fast-twitch rat muscle, this regulation of G_M has two distinct phases. At the onset of AP firing, Phase I involves the inhibition of ClC-1 channels through a PKC-mediated mechanism causing a decline in G_M to ~40% of its resting value. Then, during prolonged activity, Phase II changes involve the opening of ClC-1 and K_{ATP} channels, increasing G_M to four to five times its value in quiescent fibers. Upon cessation of AP firing, G_M recovers to its level before AP firing in 1–5 min.

In our companion paper (see Pedersen et al. in this issue), we demonstrated the significance of this G_M regulation for subthreshold electrical properties in muscle fibers, and from this predicted the effects of such G_M changes upon their excitability. In particular, our study described the relative sensitivity of the different aspects of muscle excitability, including neuromuscular transmission, sarcolemmal AP propagation, and tubular (t)-system excitation, to such regulation. The study used a linear circuit analysis appropriate for subthreshold electrical membrane phenomena. This approach first allowed for the development of analytical solutions for three cable models of muscle fibers. To determine which of these models gave the best representation of the electrical properties of rat extensor digitorum longus (EDL) muscle fibers in which the G_M regulation has been observed, experimental measurements of membrane impedance properties were compared with the electrical characteristics of the cable models. This demonstrated that circuit models of rat EDL muscle fibers require a substantial luminal t-system resistance to account for experimental observations of their impedance properties and the velocity with which APs propagate in these fibers.

Correspondence to James A. Fraser: jaf21@cam.ac.uk

Abbreviations used in this paper: AP, action potential; CD, charge–difference; ECF, extracellular fluid; EDL, extensor digitorum longus; G_M, resting membrane conductance.

The Rockefeller University Press $30.00
J. Gen. Physiol. Vol. 138 No. 1 95–116
www.jgp.org/cgi/doi/10.1085/jgp.201110617

The study went on to predict that such a luminal resistance enhances the propagation velocity of sarcolemmal APs. It also showed that a luminal resistance in series with the t-system membrane divides the voltage gradient between the intracellular and interstitial spaces into voltage drops across the t-system membrane and the luminal resistance. Because this voltage division is highly frequency dependent, the luminal resistance has important consequences for t-system excitation. Thus, high-frequency current will predominantly generate voltage gradients across the luminal resistance, whereas lower frequency components will be important for t-system excitation. The analytic approach of the previous study therefore demonstrated that G_M changes predominantly affect the low-frequency membrane impedance. It was further demonstrated, by convolving experimental APs with the circuit models, that t-system excitation is a low-frequency phenomenon that is highly dependent on G_M. Collectively, our companion study thus demonstrates that models of rat EDL muscle fibers must include a luminal resistance and suggests that neuromuscular transmission and t-system excitation are more sensitive to G_M regulation than is sarcolemmal AP propagation.

The linear circuit analysis used in our companion study was also useful in providing analytic expressions that could distinguish the appropriate equivalent circuit model for rat EDL muscle fibers and quantify the t-system luminal resistance. However, such a linear analysis is necessarily incomplete when exploring the possible physiological roles of the t-system luminal resistance and G_M regulation for the nonlinear membrane phenomena involved in AP propagation. Such nonlinear properties, explored in the present study, include voltage-dependent, time-dependent, and rectifying and Na^+/K^+-ATPase-mediated currents, as well as alterations in intracellular and t-system ionic concentrations during repetitive activity.

The aim of the present study was therefore to quantify the influence of t-system luminal resistances and G_M regulation in skeletal muscle excitability and t-system ionic homeostasis. It uses a nonlinear, iterative approach based upon the charge–difference (CD) model of Fraser and Huang (2004) and Fraser et al. (2005a,b). The development of a new model was necessary because no existing model simulates the full range of physical and electrophysiological properties that underlie t-system ionic homeostasis and its relationship with the membrane potential. Thus, early models applying circuit theory with voltage- and time-dependent conductances allow for the simulation of individual APs in the absence of ionic concentration or osmotic changes and are therefore unsuitable for simulating trains of APs where ionic concentrations shift substantially (Adrian and Peachey, 1973; Adrian and Marshall, 1976). Subsequent, more realistic models permitting the simulation of APs within the restricted extracellular space of a whole muscle (Henneberg and Roberge, 1997), and of t-system K^+ handling during AP firing (Wallinga et al., 1999), do not incorporate osmotic water movements. Therefore, they do not reach unique steady-state solutions that are independent of the initial values of key modeled variables, such as intracellular and intra–t-system ion concentrations (Fraser and Huang, 2007).

The modeling approach adopted here encompasses the known determinants of AP propagation and reaches a true history-independent steady state, thereby remaining applicable despite large perturbations in ionic concentration. It incorporates terms describing voltage- and time-dependent ion conductances and Na^+/K^+ pump activity; represents muscle fiber surface geometry using 99 linearly connected fiber segments permitting simulation of surface conduction; represents tubular geometry in terms of 20 concentric shells per fiber segment, each separated by a small luminal series resistance as was experimentally verified in our companion study (Pedersen et al., 2011); and simulates osmotic water fluxes, thereby permitting it to reach a unique history-independent steady state (Fraser and Huang, 2007).

History independence of the modeled variables was demonstrated by initiating the new model from several sets of widely divergent unphysiological values for all ion concentration variables. In each case, the model relaxed to an identical and physiologically reasonable steady state, thereby demonstrating that it was capable of investigating the determinants of intracellular and intra–t-system ionic homeostasis, and additionally allowing for the use of model-derived initial values for variables such as intra–t-system ion concentrations for which there is little available experimental data.

The initial application of this model confirmed the prediction from the preceding analytical study that the t-system luminal resistance enhances the sarcolemmal AP propagation velocity and reduces t-system excitation. It further demonstrated the influence of active AP generation within the t-system on t-system excitation and t-system ionic homeostasis, and the effect of these upon the surface membrane potential. It was then used to explore the role of G_M regulation in determining the threshold stimulus for AP firing, for t-system excitability, and for the homeostasis of K^+ ions within the t-system during repetitive AP firing. The outputs of simulated trains of APs were shown to be in close quantitative agreement with experimental intracellular recordings of AP trains obtained from rat EDL muscle fibers.

Theory

Development of a CD model of rat skeletal muscle

The electrical properties of rat EDL skeletal muscle fibers were modeled on CD principles (Fraser and Huang, 2007), adapting and extending the model of Fraser and Huang (2004) and Fraser et al. (2005a,b) to include key

nonlinear membrane phenomena of AP excitation and conduction and t-system excitation, as depicted in Fig. 1. The new model thus simulated the following features: longitudinal subdivision of the model fibers into multiple subsections connected to form a cable model; subdivision of the t-system into a series of concentric shells separated by series resistances representing the t-system luminal resistance; voltage- and time-dependent ion channels within the surface and t-tubular membranes; and ion and osmotic water fluxes across the surface and t-system membranes and the t-system luminal resistances.

The model parameters were calibrated to the passive electrical properties of rat fast-twitch EDL muscle fibers that were obtained using the analytic model in our companion study (Pedersen et al., 2011). This allowed its subsequent use in evaluating the physiological significance of the t-system luminal resistance and G_M regulation in active muscle fibers that has been observed previously in AP-firing EDL fibers (Pedersen et al., 2009a). The model was developed to adhere strictly to four key principles: (a) current continuity; (b) conservation of charge and mass; (c) electrodiffusion of ions; and (d) osmotic equilibrium at steady state.

(a) The principle of current continuity across the resistances and capacitances of the CD model. The simulation of multiple apposing finite compartments within strict conservation principles requires that any flow of current completes a circuit to ground, and also that such currents, whether capacitative or resistive, correlate precisely with the correct changes in compartmental ion contents. Both current continuity and conservation principles can be achieved straightforwardly for ionic fluxes through ion channels and across resistances by the following equations:

$$\Delta[S]_a = J_S A_{m(a)} \Delta t, \ (\text{mol l}^{-1}\text{s}^{-1}),$$

$$\Delta[S]_b = -J_S A_{m(b)} \Delta t, \ \left(\text{mol l}^{-1}\text{s}^{-1}\right).$$

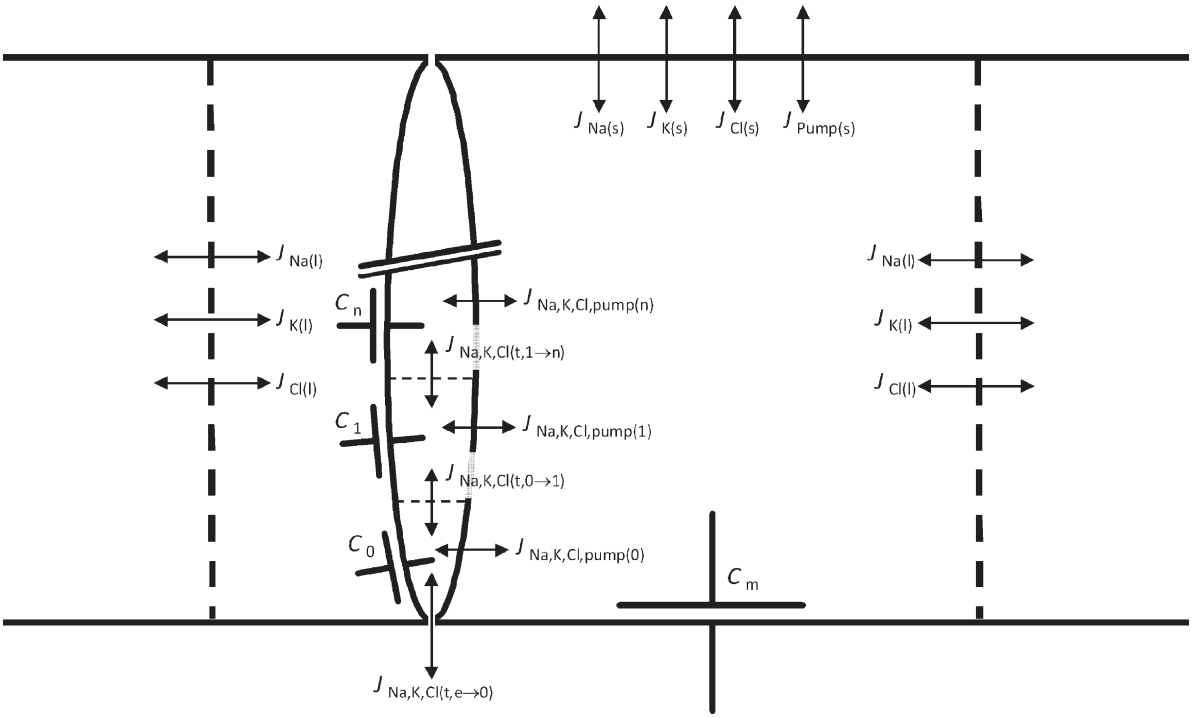

Figure 1. The ionic fluxes and capacitances simulated in the CD model of skeletal muscle cable properties. A multi-compartment model was developed to model the cable properties of skeletal muscle. The muscle fiber was divided into 99 longitudinal segments, the length of which could be varied. Each cable segment contained a t-system compartment that could be simulated as a single compartment or further subdivided into several concentric shells. In each cable segment, ionic fluxes through background and voltage-gated ion channels, calculated using the Goldman equation, and Na^+/K^+-ATPase (pump) fluxes were simulated across the sarcolemma membrane (J_s), and across the membrane of each t-system shell (J_n). Ionic fluxes across the t-system access resistance ($J_{t(e\to0)}$), between t-system shells ($J_{(n\to n+1)}$), and between adjacent cable segments of the muscle fiber ($J_{(l)}$) were calculated using an electrodiffusion equation according to the prevailing concentration and electrical gradients. In addition to the depicted ionic currents, water fluxes were also modeled, allowing the model to reach a steady state that is independent of the initial concentration of any ion. Potential differences were calculated, as described in the Theory section, across the surface membrane capacitance (C_m), across the membrane capacitance of each t-system shell (C_n), between each cable segment, between the extracellular space and the outer shell of the t-system, and between each t-system shell.

where $[S]$ represents the concentration of any solute (mol l^{-1}), the subscripts a and b denote the compartments between which the ionic flux, J (mol cm^{-2}), is flowing, and A_m is the membrane area per unit volume ($cm^2\,l^{-1}$) for each compartment. Conservation of charge and ion concentration is clear from the relationship $\Delta[S]_a/A_{m(a)} = -\Delta[S]_b/A_{m(b)}$.

The CD modeling approach additionally permitted calculation of the less straightforward requirement to characterize the precise ionic concentration changes resulting from capacitive currents, in which association of one ion species with one "plate" of a capacitor might displace or attract different ion species from or to the other plate, such that $\Delta[S]_a/A_{m(a)} \neq -\Delta[S]_b/A_{m(b)}$, in marked contrast to the situation with currents through ion channels. For example, hyperpolarization of the t-tubular membrane could result in the association of Na^+ and/or Cl^- dissociation with the outer membrane surface, but the dissociation of K^+ from the inner membrane surface. This possibility is made explicit by the following relationships for the surface and t-tubular membrane capacitance (C_m, F cm^{-2}) in a muscle fiber with a homogenous t-tubular compartment separated from the bulk extracellular fluid (ECF) by an access resistance, R_A:

$$E_m = Q_{sm} / (C_m A_m),\ (V)$$

and:

$$E_t = Q_{tm} / (C_m A_t),\ (V)$$

while:

$$E_A = E_m - E_t,\ (V)$$

where Q_{sm} is the net charge associated with the surface membrane capacitance, Q_{tm} is the net charge associated with the t-system membrane capacitance, with each expressed per liter of cell volume (C l^{-1}), and A_m and A_t represent the membrane areas of the sarcolemma and t-system, respectively, referred to total cell volume ($cm^2\,l^{-1}$). E_m represents the trans-sarcolemmal membrane potential, E_t is the trans-tubular membrane potential, and E_A is the potential across the tubular access resistance. Ionic fluxes then directly influence the ion concentrations and hence the net charges within the intracellular (i) and t-tubular (t) compartments. These relate to the charges associated with membrane capacitances by:

$$Q_i = Q_{sm} + Q_{tm},\ (C\,l^{-1})$$

$$Q_t = -Q_{tm}.\ (C\,l^{-1})$$

These relationships encapsulate the principles that (a) intracellular charge may be associated with either C_m or C_t; and (b) any deposition of charge on one plate of C_t must be matched by an equal charge flowing from its opposing plate. These relationships incorporate the assumptions that (a) the outer surface of C_m is grounded via a pathway of insignificant resistance; and (b) the outer surface of C_t is grounded via a nonzero access resistance, R_A, thereby allowing E_m and E_t to differ. Collectively, these assumptions imply that any alterations in Q_t, for example because of currents across R_A, are matched by equal alterations in charge on C_m, thereby completing a circuit to ground.

(b) Strict conservation principles in CD modeling of multiple interconnected finite compartments. By tracking concentration changes and then calculating electrical potentials directly from the concentrations of charge carriers and the associated capacitance terms, the CD approach results in a model that obeys fundamental charge and mass conservation principles. This allows the model to reach true steady states that are independent of the initial values of any modeled variable (Fraser and Huang, 2007). Thus, for a single membrane-bound compartment, the electrical potential with respect to the bulk ECF is given at any time by:

$$E_m = Q_i / C_m,\ (V)$$

where E_m is the membrane potential, and C_m is the membrane capacitance. Q denotes net charge, and the subscript "i" denotes the intracellular space, such that:

$$Q_i = F([Na^+]_i + [K^+]_i - [Cl^-]_i + z_X[X]_i),\ (C\,l^{-1})$$

where z_X is the mean charge valency of the various membrane-impermeant solutes, denoted X, and F is Faraday's constant. The influence of z_X and $[X]_i$ on the steady state of the model has been described previously (Fraser and Huang 2004, 2007; Fraser et al., 2005a).

With the current–continuity assumptions explored above, relationships may be given for E_m and E_t in terms of the CDs within each compartment. First, if the t-system is considered as a single homogenous compartment, partially bounded by a membrane with capacitance per unit area that is identical to that of the surface membrane, then:

$$E_m = \frac{([Q]_i + [Q]_t V_t)}{(C_m A_m)},\ (V)$$

$$E_t = \frac{-[Q]_t V_t}{C_m A_t},\ (V)$$

$$[Q]_i = F([Na]_i + [K]_i - [Cl]_i + z_X[X]_i)$$
$$[Q]_t = F([Na]_t + [K]_t - [Cl]_t + [Z]_t),\qquad C\,l^{-1}$$

where V_t is the volume of the t-system relative to the cell volume, V_c; and $Z_{(t)}$ denotes the fixed charge density within the t-tubules (C l^{-1}). It is implicit in these equations that the ionic activities of the mobile ions are 1. Sign conventions are as follows: the surface membrane potential (E_m) is expressed as the potential of the intracellular space with respect to the ECF; and the t-system membrane potential ($E_{t(n)}$) is expressed as the potential of the intracellular space with respect to the potential of the t-system lumen in each shell, n.

To calculate transmembrane potentials when the t-system is modeled as multiple concentric shells, the excess charge within the t-system is simply summed, thus:

$$E_m = \frac{\left([Q]_i + \sum_{n=0}^{N} [Q]_{t(n)} V_n\right)}{(C_m A_m)}, \text{ (V)}$$

$$E_{t(n)} = \frac{-[Q]_{t(n)} V_t}{C_m A_t}, \text{ (V)}$$

where V_n (dimensionless) is the volume of each t-system shell, n, relative to the cell volume, and V_t is the volume of the t-system relative to cell volume.

(c) Electrodiffusion of ions. In all cases, ionic movements were calculated according to both the concentration gradient and the local electrical gradient. This contrasts with previous models of skeletal muscle fibers that consider either diffusional fluxes or electrical currents across t-system luminal resistances, but not both (Falk and Fatt, 1964; Freygang et al., 1964; Adrian and Peachey, 1973; Adrian and Marshall, 1976; Henneberg and Roberge, 1997). However, preliminary simulations demonstrated that AP activity resulted in alterations in both t-system ion concentrations and t-system electrical potential, thereby necessitating the simulation of both diffusional and electrically driven ion movements.

Transmembrane ionic fluxes were calculated using the Goldman flux equation (Goldman, 1943). Fluxes across R_A and between t-system shells were calculated as the sum of electrical drift and diffusional fluxes:

$$J_{S((n-1)\to n)} = \left(\frac{V_t \sigma_t A_n}{\Delta}\right)\left(g_{t(n)} \frac{[S]_n}{[C]_n} \frac{E_{t(n-1)} - E_{t(n)}}{z_S F} + D\left([S]_{(n-1)} - [S]_{(n)}\right)\right), \left(\text{mol s}^{-1}\right)$$

where σ_t is the t-system tortuosity factor (Wallinga et al., 1999) (dimensionless); A_n is the area of shell n (dm^2); Δ is the distance between successive t-system shells (dm); g_t is the inter-shell conductance (S dm^{-1}) for shell n; $[S]_n/[C]_n$ is the concentration of S relative to the total mobile ion concentration within shell n (dimensionless), such that each ionic species, S, contributes an appropriate proportion of the total conductance; and D is the diffusion coefficient (dm^2 s^{-1}), assumed to be equal for all modeled ions.

Fluxes across R_A were calculated as follows:

$$J_{S(e\to 0)} = A_m \left(\frac{D}{R_A g_t}\left([S]_e - [S]_0\right) + \frac{[S]_0}{[C]_0}\left(\frac{-E_0}{R_A z_S F}\right)\right), \left(\text{mol l}^{-1}\text{s}^{-1}\right)$$

where the $D/R_A g_t$ term ensures that the ratio between the diffusive and electrical components of the flux across R_A is equal to that between t-system shells.

(d) Osmotic equilibrium at steady state. Fraser and Huang (2004, 2007) showed that when the steady state of a CD model cell is constrained by the requirement for osmotic equilibrium at steady state, then the steady-state values of these variables were uniquely defined by the permeabilities and extracellular concentrations of each ion and by the Na^+/K^+ pump density. Furthermore, certain concentrations are tightly constrained at osmotic equilibrium. For example, when Cl^- is the only extracellular anion and therefore contributes half of the extracellular osmolality, $[Cl^-]_t$ must be equal to $[Cl^-]_e$ for t-system osmolality to be equal to extracellular osmolality. Thus, osmotic water movements are fundamental to ensure accurate steady-state behavior that is constrained to what is physically possible. This allows CD modeling to be used to simulate manipulations expected to have a large influence on ion concentrations, in contrast to models that do not reach true steady states (Fraser and Huang, 2007). Thus, transmembrane water fluxes were calculated as:

$$J_{H2O(a\to b)} = A_m P_{H2O} (\Pi_b - \Pi_a),$$

where Π is the osmolality of each compartment and P_{H2O} is the hydraulic permeability of the membrane, taken as 156 μm s^{-1} (Frigeri et al., 2004). Water fluxes across R_A and between t-system shells were assumed to be instantaneous to maintain osmotic equality in all extracellular compartments.

It is clear from the profound changes in t-system volume with manipulations of extracellular ion concentrations or osmolality (Rapoport et al., 1969; Dulhunty, 1982; Chawla et al., 2002) that the t-system cannot be treated as a rigid structure. The model therefore allowed the t-system volume to be determined by the balance of osmotic fluxes across the t-system membrane and R_A. This gave stable steady-state values when a small fixed negative charge term was included in the t-system and responded appropriately to changes in extracellular osmolality in preliminary experiments (unpublished data).

Simulation of cable properties and AP firing

A length of muscle fiber was simulated as 99 identical segments. Ion concentrations and membrane potentials were calculated for each segment as described above. Inter-compartment ion fluxes were calculated for each intracellular ionic species according to the prevailing electrical gradient between segments:

$$J_{S(x\rightarrow(x+1))} = \frac{A_x}{R_L z_S F V_x}\left(\frac{E_{m(x)} - E_{m(x+1)}}{\Delta L}\right), \text{ (mol dm}^{-3}\text{s}^{-1}\text{)}$$

where A_x is the membrane area of compartment x (dm^2), V_x is its volume (dm^3), R_L is the longitudinal resistance, and ΔL is the distance between the centers of adjacent compartments. As each segment was identical, ion concentrations did not differ significantly between adjacent segments; therefore, it was not necessary to include a diffusional flux term.

The simulations were performed using a 100-µm segment length. Initial simulations to determine the optimal segment length compared the behavior of model fibers with 100-µm segment lengths to those with 10-µm segment lengths. Over a range of frequencies from 25 to 3,000 Hz, frequency–velocity relationships for passive sinusoidal currents were not influenced by this change in segment length (difference in velocity <1% at each frequency; not depicted).

APs were modeled by adding voltage-gated Na^+ and K^+ channels to the surface and t-tubular membranes. Voltage-gated ion channels were simulated using Hodgkin–Huxley gating equations (Hodgkin and Huxley, 1952), with conductances and gating parameters calibrated to rat skeletal muscle (Cannon et al., 1993; Henneberg and Roberge, 1997; Wallinga et al., 1999). Nevertheless, the present model differs significantly from these existing models in several important respects. First, all modeled variables, including t-system ion concentrations and ion channel–gating variables, reach stable steady-state values that are independent of initial conditions. In contrast, these existing models treat some or all ion concentrations as fixed parameters. Second, the present model simulates ion diffusion between the t-system and extracellular space according to the prevailing electrical and concentration differences. In contrast, existing models simulate passive diffusion, yet particularly when E_t lags E_m during the early phase of the surface AP, the voltage between the t-system and the ECF was shown to reach almost 100 mV in these earlier studies (Wallinga et al., 1999).

A stimulus was required to initiate APs. This was applied to the central compartment in the cable model. To maintain strict conservation principles, stimulation currents were simulated as fluxes of K^+ and Cl^- of equal

TABLE I

Summary of physical and electrophysiological parameters used

Symbol	Description	Value	Reference
Physical parameters			
A_m	Surface membrane area	769231 $cm^2\,l^{-1}$	1
A_t	t-System membrane area	3076924 $cm^2\,l^{-1}$	1
V_t	Relative t-system volume	3.2e-3 liter.l^{-1}	2, 7
C_m	Membrane capacitance	1e-6 F cm^{-2}	1
R_a	t-System access resistance	72.3 Ω cm^2	1
R_i	Longitudinal fiber resistance	180 Ω cm	1
g_t	t-System luminal conductance	3.7e-3 S cm^{-1}	2
σ_t	t-System tortuosity factor	0.21	2
Electrophysiological parameters			
N_s	Na^+/K^+-ATPase sarcolemmal density	9e-12 cm^{-2}	3
N_t	Na^+/K^+-ATPase tubular membrane density	4.5e-12 cm^{-2}	3
P_{Na}	Background Na^+ permeability	2.16e-8 cm s^{-1}	4, 5
P_K	Background K^+ permeability	6.3e-7 cm s^{-1}	4, 6
P_{Cl}	Background Cl^- permeability	2.7e-6 cm s^{-1}	4, 6
$P_{Na(v,s)}$	Voltage-gated Na^+ channel sarcolemmal permeability	0.00265 cm s^{-1}	7
$P_{Na(v,t)}$	Voltage-gated Na^+ channel t-system permeability	0.00034 cm s^{-1}	7
$P_{K(v,s)}$	Voltage-gated K^+ channel sarcolemmal permeability	0.0004 cm s^{-1}	7
$P_{K(v,s)}$	Voltage-gated K^+ channel t-system permeability	0.0001 cm s^{-1}	7

References: 1, Pedersen et al., 2011; 2, Wallinga et al., 1999; 3, model derived to maintain $[Na^+]_i$ in physiological range; 4, total conductance taken from Pedersen et al. (2011); 5, P_{Cl}/P_K ratio (Dulhunty, 1979; Pedersen et al., 2005); 6, P_{Na}/P_K ratio model derived to obtain membrane potentials in agreement with control experiments; 7, Henneberg and Roberge, 1997. Hodgkin-Huxley parameters for voltage-gated Na^+ and K^+ channels are from Henneberg and Roberge (1997). Note that all intracellular ion concentrations and compartmental volumes in the model are variables, the values of which are determined solely by the choice of parameters, as demonstrated in Fig. 2. Extracellular Na^+ and K^+ concentrations matched those of the experimental studies, and extracellular $[Cl^-]$ was chosen to make the solution electroneutral.

magnitude and opposite direction, thereby approximating stimulation with a KCl-filled microelectrode.

Calibration to rat skeletal muscle

The physical conductance parameters summarized in Table I were calculated from experimental measurements of subthreshold sine wave conduction using the analytic model of Pedersen et al. (2011). Resting membrane permeabilities for Na^+, K^+, and Cl^- were calculated from membrane conductance measurements, literature values for the ratio P_{Cl}/P_K, and model fitting of E_m to the present experimental data for the P_{Na}/P_K ratio. Unless otherwise stated, the ionic permeabilities per unit area of the t-system membrane and the sarcolemma were assumed to be identical. The Na^+/K^+ pump was simulated using the model of Hernandez et al. (1989), and its membrane density was chosen to produce reasonable resting values of $[Na^+]_i$. Finally, voltage-gated channel permeabilities, distribution, and kinetics were as described by Henneberg and Roberge (1997).

Model initiation and validation

A critical advantage of CD modeling is that E_m, E_t, and all intracellular and intra–t-system ion concentrations are dependent variables that have unique steady-state values for any given set of physical, permeability, and pump parameters. Therefore, the model may be initiated with arbitrary values of the principal modeled variables ($[Na^+]_i$, $[K^+]_i$, $[Cl^-]_i$, $[X]_i$, $[Na^+]_t$, $[K^+]_t$, $[Cl^-]_t$, and $[Z]_t$). In the present study, the model was run to steady state from two markedly different semi-arbitrary sets of these variables using a single physiological parameter set as listed in Table I. As shown in Fig. 2, the eventual steady-state values of all modeled variables were identical in each case. This demonstrates that the new model fully obeys conservation principles. Furthermore, the eventual steady-state values of all variables are physiologically reasonable and in agreement with published data, thereby providing some validation of the model. This procedure was also used to obtain the steady-state values in the multiple-shell t-system model (unpublished data), similarly demonstrating a unique steady-state independent of the starting values of the variables.

MATERIALS AND METHODS

Animal handling

Experimental recordings of trains of APs were obtained from surface muscle fibers of intact EDL muscles from 12-wk-old female Wistar rats of our own breed (~230 g). Animals were kept at 21°C and fed ad libitum living under 12:12-h light/dark conditions. All handling and killing of animals followed Danish welfare regulations. After dissection, the muscles were incubated in standard Krebs-Ringer bicarbonate solution (pH 7.4 at 30°C) containing (in mM): 122 NaCl, 25 $NaHCO_3$, 2.8 KCl, 1.2 KH_2PO_4, 1.2 $MgSO_4$, 1.3 $CaCl_2$, and 5.0 D-glucose. All solutions were equilibrated with a mixture of 95% O_2 and 5% CO_2.

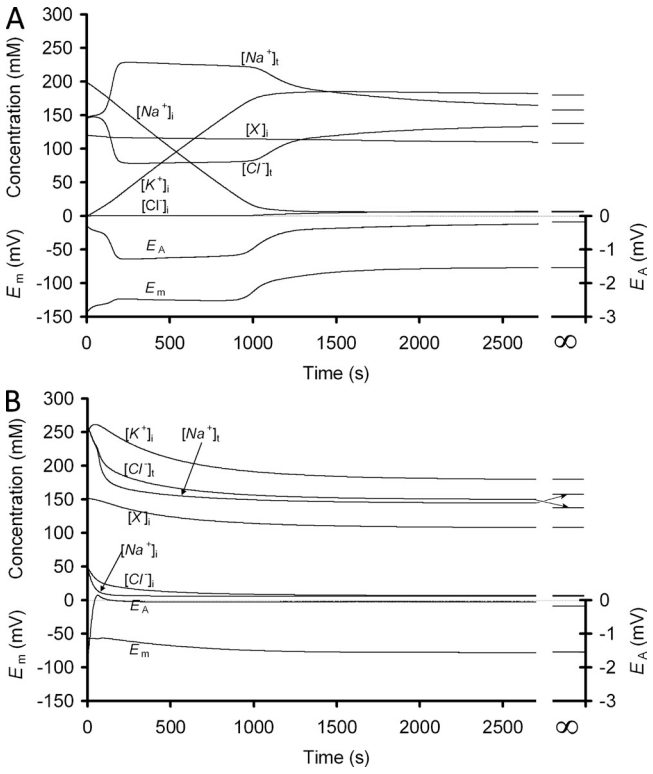

Figure 2. The model cell reaches a single physiologically reasonable steady state that is independent of the initial values of any modeled variable. All variables are plotted on the left-hand scales, except for the potential across the t-system access resistance (E_A, broken line), which is plotted on the right-hand scale. The model was initiated using physiological parameters (Table I), but with two sets of intracellular ion concentrations that were chosen to be markedly different from each other and clearly unphysiological, although fulfilling a constraint of bulk electroneutrality in each compartment. See Table II below for a summary of the initial and steady-state values of the major modeled variables.

Recordings of trains of APs

Trains of APs were recorded using a two-microelectrode setup described in detail previously (Pedersen et al., 2005). In brief, two sharp electrodes (~20 MΩ) were inserted into the same muscle fiber, and the train of APs was initiated by injecting an ~3.5-s train of constant current pulses (3 ms, 300 nA) into the fiber through

TABLE II

From legend to Fig. 2

Variable (units)	Initial value 1	Initial value 2	Final value 1	Final value 2
$[Na^+]_i$ (mM)	200	50	5.84	5.84
$[K^+]_i$ (mM)	0	250	180.3	180.3
$[Cl]_i$ (mM)	0	50	7.37	7.37
$[X]_i$ (mM)	121.4	151.7	108.5	108.5
$[Na^+]_t$ (mM)	0	0.01	157.6	157.6
$[K^+]_t$ (mM)	0.01	1	6.38	6.38
$[Cl]_t$ (mM)	0	1.009	138.0	138.0
$[Z]_t$ (l^{-1})	−0.01	−0.001	−25.4	−25.4

Note that the final value of each modeled variable, shown at time ∞ in Fig. 2, is both physiologically reasonable and independent of its initial value.

one electrode while the other electrode recorded the membrane voltage. To allow the electrodes to remain inserted during AP trains, contractile activity of the muscle fibers was reduced by including 50 μM of the specific MHC II inhibitor, *N*-benzyl-*p*-toluene sulphonamide (BTS), to the Ringer's solution as described by Macdonald et al. (2005).

RESULTS

Our companion study (Pedersen et al., 2011) demonstrated that linear electrical circuit models must incorporate a significant t-system luminal resistance to accurately model the subthreshold electrical properties of rat EDL muscle fibers. It was possible to evaluate the physiological significance of such resistances for sarcolemmal AP propagation velocity and t-system excitation. This led to an evaluation of the role of G_M regulation during repetitive firing of short AP trains (Pedersen et al., 2009a). The present study proceeded to a quantitative analysis of important nonlinear responses not amenable to the preceding analytic methods of Pedersen et al. (2011) using a new nonlinear model based on CD modeling principles (Fraser and Huang, 2004; Fraser et al., 2005a,b). First, the frequency dependency of the conduction velocity of passively conducted sine waves was quantified in the new CD model and compared with the previous findings based on linear current–voltage relationships (Pedersen et al., 2011). Second, the influence of voltage- and time-dependent ion channels within both the surface and t-system membranes was clarified. Third, this permitted an analysis of t-system ion concentration changes and their influence upon surface and t-system membrane potential and excitability during repetitive AP firing. Experimental microelectrode recordings of membrane potential were compared with the results of the CD modeling.

Passive conduction properties of skeletal muscle fibers

Fig. 3 A demonstrates the relationship between frequency and passive conduction velocity in simulations without voltage-gated ion channels under four different degrees of separation of the t-system from the true ECF. Fiber properties were simulated assuming: (a) no R_A (simple cable model); (b) a physiological R_A of 72.3 Ω cm^2 (homogenous t-system model; equivalent to the lumped model of Pedersen et al., 2011); (c) physiological R_A and additional smaller series resistances (3.7 mS cm^{-1}; Wallinga et al., 1999) between each of 20 concentric t-system shells (20-shell t-system model, equivalent to the distributed cable model in Pedersen et al., 2011); and (d) extremely high R_A (723 Ω cm^2) simulating near-complete isolation of the t-tubules from the ECF (detubulation model).

In full agreement with the findings of our companion analysis (Pedersen et al., 2011), the homogenous t-system model showed faster conduction than the simple cable model, particularly at higher frequencies. This was despite the fundamentally different assumptions and approaches underlying the two models. The 20-shell t-system model (Wallinga et al., 1999) similarly showed faster conduction velocity <1,000 Hz, but slightly slowed

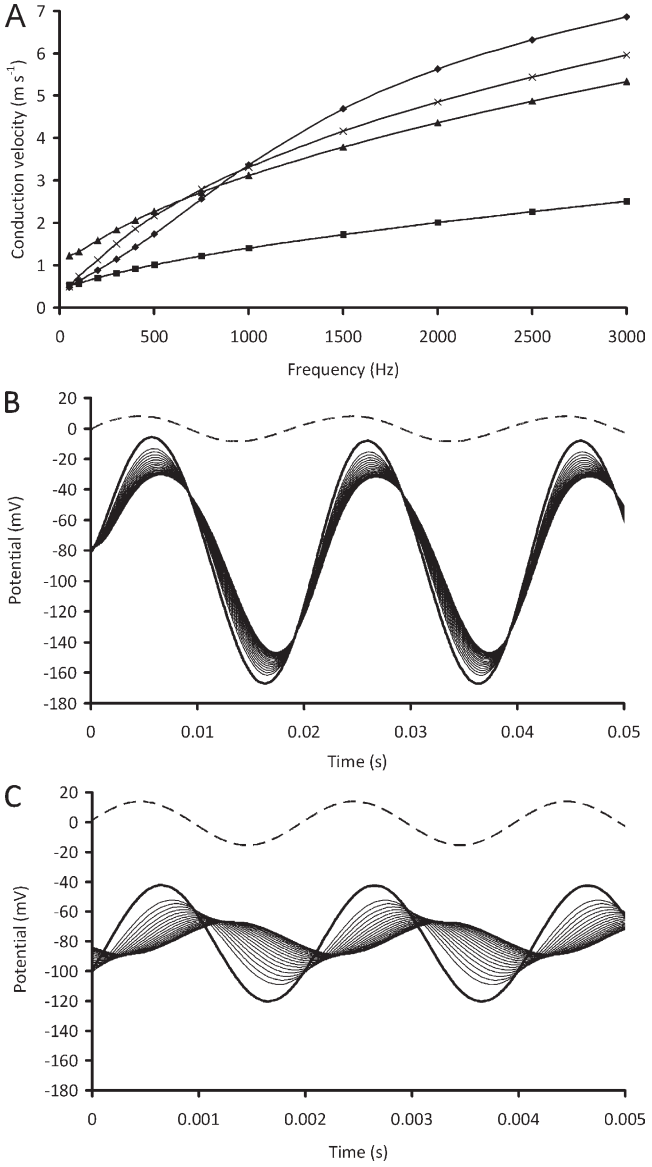

Figure 3. The influence of t-system access and luminal resistances upon the conduction velocity of a passively propagated sine wave and associated t-system potential changes. (A) The frequency–velocity relationships for model muscle fibers with: no resistance between the ECF and the t-system lumen (squares); an extremely high access resistance, simulating detubulation (triangles); a physiological t-system access resistance between a single homogenous t-system compartment and the ECF (diamonds); and a physiological t-system access resistance and smaller physiological resistances between each of 20 concentric t-system shells (crosses). Sine waves were driven by a sinusoidal ±300-nA current carried by K^+ and Cl^- ions. (B and C) The underlying changes in E_m (thick lines), E_A (dashed lines), and $E_{t(0–19)}$ (lighter lines, from E_0, closest to E_m, to E_{19}, furthest from E_m) in the 20-shell t-system model during stimulation at 50 Hz (B) and 1,000 Hz (C). Note that the potential across $E_{t(0–19)}$ closely tracks E_m at 50 Hz, but lags E_m in both phase and amplitude at 1,000 Hz.

conduction velocity >1,000 Hz, relative to the homogenous t-system model. It is interesting to note that both physiological R_A and intra–t-system series resistances appear to enhance the conduction velocity at frequencies corresponding to those of the AP upstroke (Pedersen et al., 2011). Further increases in R_A to yield a detubulation model produced further accelerated conduction at lower frequencies (<600 Hz) but slowed conduction at all higher frequencies relative to fibers with a physiological R_A, regardless of whether additional intra–t-system resistances were present.

Fig. 3 (B and C) demonstrates the changes in t-system transmembrane voltage, E_t, and the voltage across the sarcolemma, E_m, during sine wave propagation. In full agreement with the analytical solutions of our companion study, the CD model demonstrates that the voltage division of the intracellular potential between the t-system membrane and R_A is highly frequency dependent. Thus, at low frequency (50 Hz; Fig. 3 B), E_t tracks E_m relatively closely, indicating that the t-system membrane then dominates the impedance path from the cytosol through the t-system to the ECF. At higher frequency (1,000 Hz; Fig. 3 C), the amplitude of E_t is significantly reduced relative to that of E_m, corresponding to R_A rather than the t-system membrane progressively dominating this impedance path. The larger voltage drop across R_A when compared with that across the t-system membrane at high frequencies has two consequences. First, the t-system membrane is poorly charged by high-frequency components of the circuit currents during AP propagation. Second, because current and voltage do not lag on a resistive component, R_A reduces the phase lag between current and voltage at such frequencies. This reduces the time required for high-frequency currents important for AP propagation to charge the sarcolemma. This latter point explains the steeper frequency–velocity relationship observed in models possessing a t-system luminal resistance (Fig. 3 A) and furthermore, as in the previous linear analysis, suggests that R_A causes the sarcolemmal AP to propagate faster.

The similarities in frequency–velocity relationships shown by the CD and linear circuit models (Pedersen et al., 2011) occurred despite the distinctly nonlinear current–voltage relationships for each ionic current and the resultant total currents in the former. These nonlinearities result from the differing intracellular and extracellular concentrations of the major transmembrane charge carriers, K^+ and Cl^-, resulting in equivalent membrane resistances varying from 2.0 to 5.3 kΩ in the surface membrane and 0.6 to 1.3 kΩ in the t-system during the 50-Hz sine wave, in each case with the lower resistances occurring with greater depolarization. Thus, the nonlinearity of background current–voltage relationships does not influence passive conduction velocity.

Conduction velocity of actively propagated signals in skeletal muscle fibers

The findings above thus demonstrate that CD modeling successfully reproduces experimental measurements and linear modeling of passive frequency–velocity relationships in EDL muscle fibers (Pedersen et al., 2011). Thus, the simulations of passive conduction demonstrate that increased signal frequency, and increased R_A at frequencies below ∼800 Hz, each produce a greater conduction velocity, but also decreased t-system excitation. However, AP conduction velocities in skeletal muscle under physiological conditions depend upon a combination of passive signal propagation and active signal regeneration. Furthermore, coordinated excitation–contraction coupling along the entire length of a muscle fiber requires both rapid AP conduction and t-system excitation. Simulations of regenerative AP conduction were therefore performed to: (a) determine the influence of active regeneration upon the conduction velocity of surface APs; (b) investigate the influence of R_A and the presence or otherwise of voltage-gated channels within the t-system upon AP conduction velocity and t-system excitation; and (c) investigate the influence of the G_M changes observed during repetitive AP firing on surface and t-system excitability.

The influence of active signal regeneration upon conduction velocity. Fig. 4 demonstrates the importance of active signal regeneration to sarcolemmal conduction velocity. It displays results from two model fibers with physiological densities of voltage-gated Na^+ and K^+ channels after stimulation in the central of 99 compartments into which the fiber long axis was divided. Fig. 4 A compares voltage responses in six adjacent compartments 3–3.5 mm from the initial stimulus along each model fiber. The solid lines depict results from a model fiber with a physiological density of voltage-gated ion channels. The broken lines depict the passive conduction remaining when the permeabilities of the voltage-gated ion channels in all compartments beyond 3 mm from the stimulus were fixed at their resting values. The latter shows that signal amplitude steeply declines with distance, reflecting an absence of active signal regeneration. Furthermore, the increased spacing of the peaks with distance in the passive conduction model (marked by vertical broken lines) indicates a marked deceleration of the passively propagated signal with distance from its source, relative to the actively propagated signal.

Fig. 4 (B–D) goes on to examine the detailed effects of P_{Na} upon the conduction characteristics. Fig. 4 B (inset) shows AP traces resulting from setting the maximum permeability of the voltage-gated Na^+ channel ($P_{Na(max)}$) at 200% (*i*), 100% (*ii*), 50% (*iii*), or 30% (*iv*) of the value expected under control conditions (Henneberg and Roberge, 1997). The AP magnitude increased and the time to peak decreased with increasing $P_{Na(max)}$.

The resulting sarcolemmal conduction velocity of actively propagated APs (Fig. 4 B, squares) then showed a log-linear dependence upon $P_{Na(max)}$, similar to the relationship between passive conduction velocity and sine wave frequency (Fig. 3). This contrasted with the shallower dependence on $P_{Na(max)}$ of the velocity of passively conducted AP waveforms over the first 100 µm ahead of the active AP wave front. This is consistent with the highest frequency, fastest conducting components of the AP having the shortest length constants (Pedersen et al., 2011).

Fig. 4 C summarizes a power spectral analysis of the AP traces in the inset of Fig. 4 B obtained by their Fourier transformation to permit a comparison of their frequency content and the conduction velocity of the corresponding APs. It clearly correlated an increased $P_{Na(max)}$ with a larger content of high-frequency components in the resulting AP waveforms. This could be compared directly with the frequency dependence shown by the propagation velocity of passive subthreshold sinusoidal voltage changes, through identification of an equivalent frequency for the AP equal to the sine wave frequency, whose conduction velocity matched that of the AP. As passive frequency components with conduction velocities slower than that of the AP cannot contribute to the AP propagation velocity,

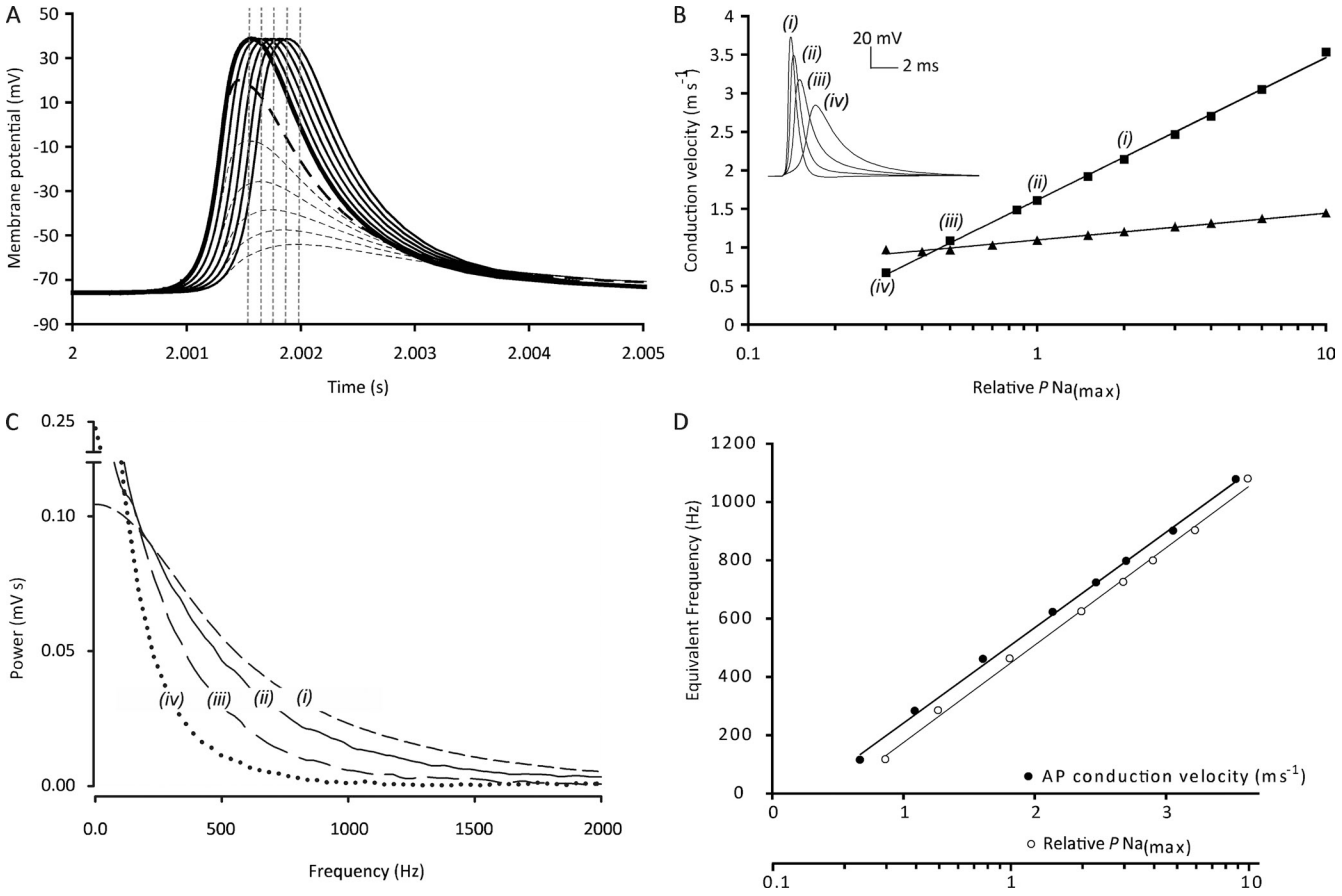

Figure 4. Comparison of passive conduction with active AP regeneration. The model with homogenous t-system was stimulated in the central of the 99 compartments at 2 s. (A) E_m over time for segments 30–35 (3–3.5 mm from the stimulus) from two simulations: in the first simulation (solid lines), active propagation persisted throughout all fiber segments; in the second (broken lines), conduction block was modeled in compartments 31 and beyond by fixing the permeability of the voltage-gated ion channels to their resting values. This allowed a direct comparison of active and passive signal propagation. The vertical broken lines mark the peaks of these passively conducted AP waveforms. It can be seen that the peaks of the passively conducted signals eventually lag the peaks of the actively propagated APs. (B) The measured peak-to-peak conduction velocity in similar simulations of conduction block, over a range of values of $P_{Na(max)}$, for actively propagated signals (squares); and for the first 100 µm of passive conduction from the final point of active regeneration (triangles). (Inset) Four traces of APs with different relative values of $P_{NA(max)}$ (*i*, 0.3; *ii*, 0.5; *iii*, 1; and *iv*, 2). The frequency content of these traces of APs was analyzed using Fourier analysis, and their power spectra are shown in C. Given that APs propagate via the spread of local circuit currents in front of the AP waveform, some elements of such passive current flow must be faster than or as fast as the active propagation. Thus, from the relation of frequency and passive conduction velocity of sinusoidal currents displayed in A, the frequency of a sinusoidal current required to match the AP propagation velocity was determined for the range of $P_{Na(max)}$ values investigated. These frequencies were referred to as equivalent frequencies. (D) This illustrates that the equivalent frequency and the active AP conduction velocity were linearly related and, furthermore, that the equivalent frequency and $P_{Na(max)}$ were log-linearly related.

this equivalent frequency therefore identifies the lowest frequency component of the circuit currents that could possibly contribute to the AP propagation velocity. Fig. 3 A was used to extract the equivalent frequencies for the different conduction velocities obtained at the different $P_{Na(max)}$ values. Fig. 4 D plots the resulting equivalent frequencies against either AP conduction velocity or $P_{Na(max)}$. The relationships were linear for the conduction velocity and log-linear for $P_{Na(max)}$ ranging from 0.3 to 10 times the control value. Collectively, these findings clearly illustrate the influence of $P_{Na(max)}$ upon the high-frequency components of the AP, and through the latter upon AP conduction velocity.

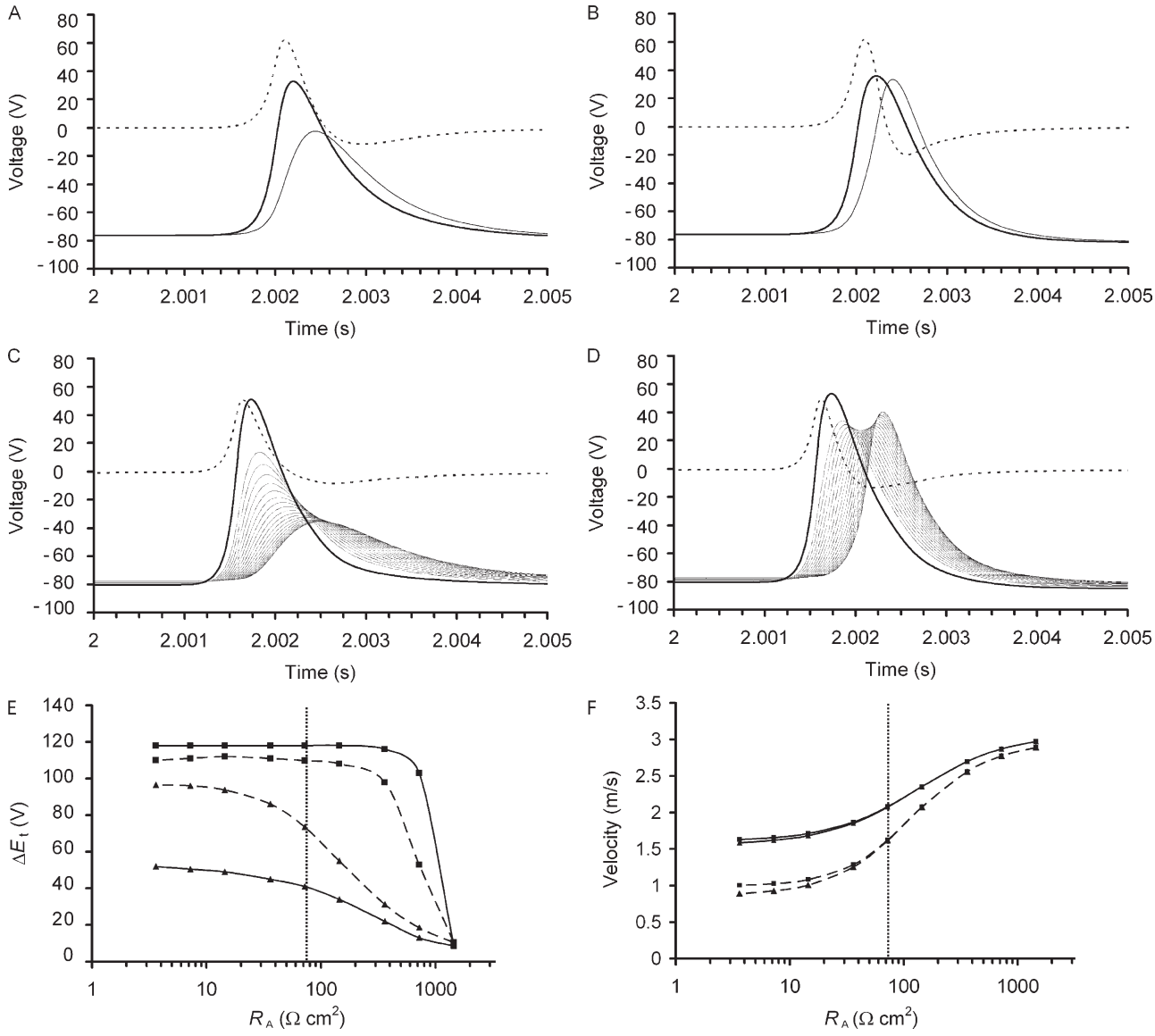

Figure 5. The influence of t-system excitability upon the t-system response to a sarcolemmal AP. The response of $E_{t(n)}$ (thin lines) and E_A (broken lines) to E_m changes (thick lines) during an AP is depicted for a model fiber with a t-system simulated as a single homogenous compartment (A and B) and for a model fiber with a 20-shell t-system (C and D). In A and C, the t-system lacks voltage-gated ion channels and therefore the voltage response is entirely passive. B and D demonstrate the response of a fiber with physiological voltage-gated ion channel densities within the t-system. Surface E_m changes are similar in each case, but the resulting tubular excitation is enhanced by the presence of voltage-gated ion channels within the t-system. (E) A summary of peak changes in fiber core E_t during the passage of a sarcolemmal AP. (F) Surface conduction velocity for fibers with (squares) and without (triangles) voltage-gated ion channels in the t-system, in the homogenous t-system model (dashed lines) and in the 20-shell t-system model, for model fibers with a range of values of R_A (solid lines). The vertical line in each case denotes the value of R_A used for the simulations in A–D. Increases in R_A reduce the passive electrical response of the t-system to the sarcolemmal AP (E) while accelerating sarcolemmal conduction velocity (F). A physiological value of R_A thus necessitates voltage-gated channels to produce a full t-system voltage response (E). Such channels have no direct effect on sarcolemmal conduction velocity (F).

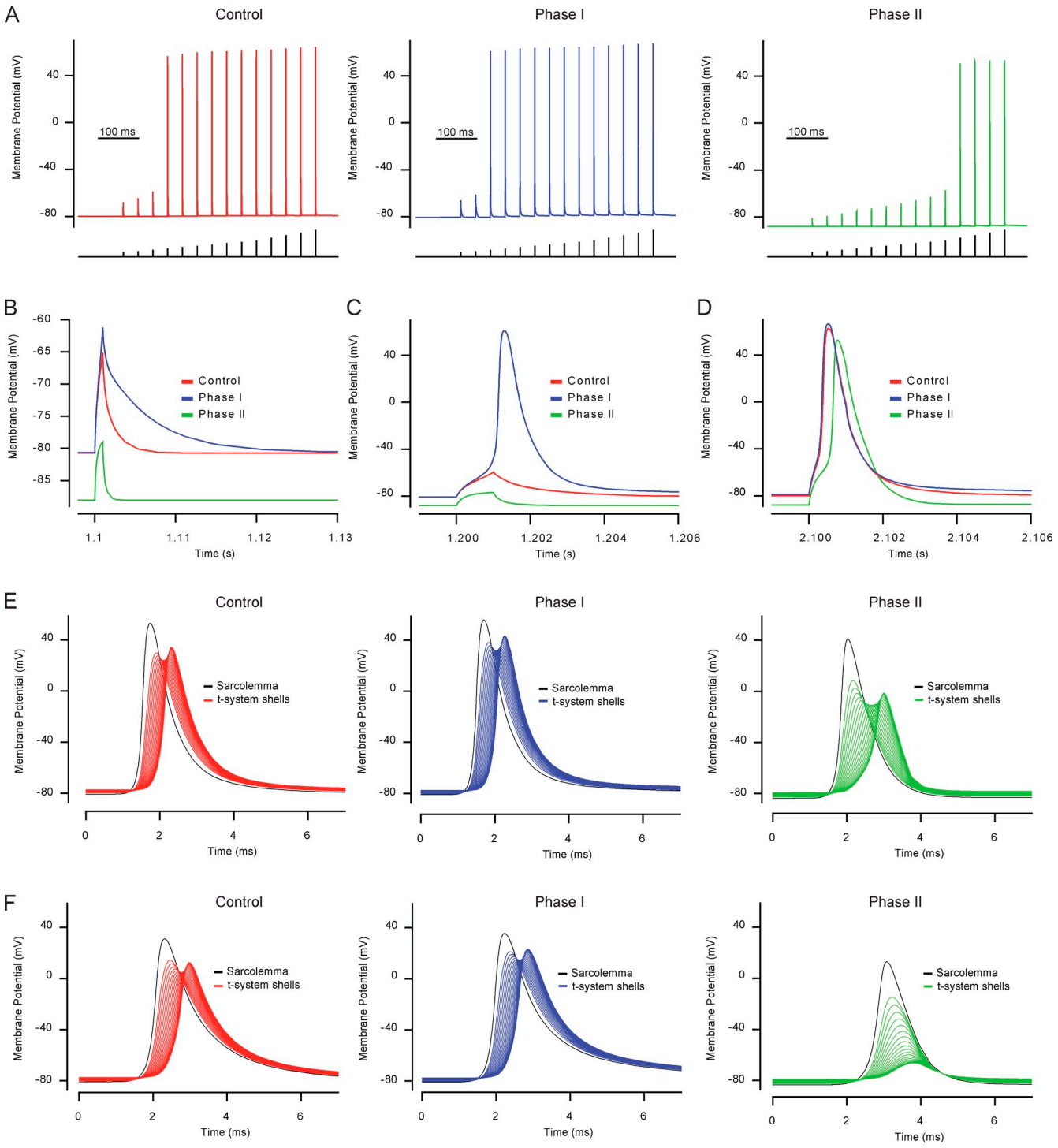

Figure 6. Effects of G_M regulation during Phase I and Phase II on simulations of excitation of sarcolemmal APs, their propagation, and t-system excitation. (A) Current flow during endplate excitation of sarcolemmal APs was mimicked by simulating injections of 1-ms square KCl currents in the central segment of the model. To determine the effect of G_M regulation on the current required to excite an AP, a range of different current amplitudes was applied. (A) The membrane potential of the central segment of the model where excitation occurred (the current injections are presented below). Membrane permeabilities of the model for K^+ and Cl^- were adjusted to mimic G_M during control conditions (left), during Phase I (middle), and during Phase II (right). (B) The membrane potential response to a current injection that did not elicit an AP under any of the conditions. Clearly, G_M regulation markedly affects the recovery of membrane potential after cessation of current injection. (C) Membrane potential under the three conditions of control, Phase I, and Phase II during the injection of a current that only triggered an AP during Phase I. (D) The membrane potential when the current amplitude was just sufficient to elicit an AP in Phase II. (E) Sarcolemmal AP (black line) and the membrane potential in the 20 t-system shells 3 mm from the point of AP excitation during control conditions (left), Phase I (middle), and Phase II (right). (F) Similar to E, but with a 50% reduction in maximum permeability for voltage-gated Na^+ channels.

The effect of t-system excitability upon surface conduction velocity and t-system excitation. The simulations depicted in Fig. 4 demonstrate that, over anything but the shortest distances, active signal regeneration by sarcolemmal voltage-gated ion channels enhances conduction velocity. The simulations that follow now analyze the effects of the voltage-gated ion channels additionally present in the t-system membrane upon t-system excitation and surface conduction velocity.

Fig. 5 compares passive (A and C) and active (B and D) t-system responses to a surface AP in a model with a single homogenous t-system compartment (A and B) and in a model with a t-system subdivided into 20 concentric shells of equal thickness (C and D). In each case, changes in $E_{t(n)}$ lag changes in E_m. In the single-compartment t-system model, the magnitude of the change in E_t (ΔE_t) is increased from +73.5 mV in the absence of voltage-gated ion channels within the t-system (Fig. 5 A) to +109.8 mV with active regeneration (B). However, findings from the 20-shell t-system model suggest that the homogenous t-system model underestimates the importance of active regeneration within the t-system. Thus, the 20-shell model shows that the E_t change in the center of the fiber ($\Delta E_{t(19)}$) is increased from +40.9 mV in the absence of voltage-gated ion channels within the t-system (Fig. 5 C) to +118.0 mV with active regeneration (D). This contrast between the two t-system models is of some relevance, as ΔE_t in the passive single-compartment t-system model would be sufficient for activation of excitation–contraction coupling, whereas $\Delta E_{t(19)}$ in the passive 20-shell t-system model is well below this activation threshold (Gallant and Jordan, 1996).

Fig. 5 (E and F) demonstrates the influence of R_A magnitude upon the peak E_t change during an AP (E), and upon the sarcolemmal AP conduction velocity (F). In the homogeneous model (Fig. 5, E and F, broken lines), an increase in R_A decreases the passive change in E_t during AP in fibers without voltage-gated ion channels in the t-system (E, triangles), but accelerates the sarcolemmal AP conduction velocity (F, triangles). Similarly, the presence of a series resistance separating successive t-system shells in the 20-shell t-system model (Fig. 5, E and F, solid lines) produces a further modest acceleration of the sarcolemmal AP (F), while greatly decreasing the passive t-system voltage response (E), relative to that of the homogenous t-system model. However, in the presence of voltage-gated ion channels in the t-system (Fig. 5, E and F, squares), the change in E_t during an AP is >100 mV in both the homogenous and 20-shell t-system models, even for values of R_A up to three times the physiological value.

Thus, these findings demonstrate that t-system luminal resistance enhances surface AP conduction at the expense of a reduced passive excitation of the t-system. However, even in the presence of a significant access resistance, voltage-gated ion channels within the t-system permit full t-system excitation during an AP. Finally, voltage-gated channels in the t-system do not contribute to the velocity of surface AP conduction.

The influence of G_M regulation in active muscle on sarcolemmal and t-system excitability. Despite the advantages of the analytical solution in generating a detailed mechanistic insight into the relationship between G_M and excitability (Pedersen et al., 2011), the approach was limited to linear analysis. The present study therefore extended the work to determine the influence of G_M changes upon muscle excitability in the presence of voltage-gated ion channels in sarcolemma and in the t-system. The simulations test the prediction that AP excitation at the neuromuscular junction and the t-system, but not along the sarcolemma, should be particularly sensitive to alterations in G_M, owing to sarcolemmal AP propagation being conveyed by high-frequency elements of the circuit currents for which the impedance of a sink membrane region would be relatively insensitive to G_M.

Thus, Fig. 6 shows the influence of Phase I and Phase II G_M changes (see Fig. 9 C) on the excitation of the sarcolemma AP. During Phase I, it was possible to trigger an AP with a current that was slightly lower than the current that triggered an AP under control conditions, whereas during Phase II, a substantially larger current was required. Thus, sarcolemmal AP excitation is facilitated by Phase I G_M regulation and markedly impaired by Phase II G_M regulation, even when excitation proceeds with currents of short durations comparable to the endplate current.

Fig. 6 B shows the subthreshold responses under each condition. G_M strongly influences the downstroke of the membrane potential response, exerting smaller influences on its upstroke and magnitude. The importance of this influence on the downstroke is demonstrated in Fig. 6 C, in which it is shown that for near-threshold stimuli, the AP upstroke occurs after the cessation of the 1-ms stimulus. Fig. 6 D additionally demonstrates that APs excited during Phase II were characterized by a reduced amplitude and slower upstroke as compared with APs during Phase I and under control conditions.

Next, sarcolemmal AP propagation and t-system excitation were simulated in the model during control conditions, Phase I, and Phase II. Fig. 6 E shows the sarcolemmal AP (black lines) and the membrane voltage in the t-system shells (red, blue, and green lines) at 3 mm from the point of excitation. Under control conditions, the simulated APs propagated at 2.03 m s^{-1}, whereas during Phase I and Phase II, it propagated at 2.09 and 1.67 m s^{-1}, respectively. Thus, Phase I caused only a 3% increase in propagation velocity, whereas Phase II reduced the propagation velocity by 18%. Under conditions when the maximum permeability of the voltage-gated Na^+ channels was reduced to 50%, the

sarcolemma propagation velocity dropped to 1.52 m s^{-1} under control conditions (Fig. 6 F). The increase in sarcolemmal AP propagation velocity during Phase I became marginally more pronounced (5%), whereas during Phase II, the sarcolemmal AP propagation velocity dropped by 36%. There were also clear-cut effects of G_M regulation on t-system excitation and t-system AP waveform. Thus, the amplitude of the AP in the innermost t-system shell became 12 and 14% larger during Phase I, whereas during Phase II, it was reduced by 19%. With reduced $P_{Na(max)}$, the t-system shells did not actually produce an AP, despite the existence of fully propagating sarcolemmal AP during Phase II. The latter finding suggests that G_M regulation during Phase II can cause loss of t-system excitation when voltage-gated Na^+ channels have been partly inactivated, as can occur through slow inactivation of these channels during repetitive AP firing. This suggests that G_M regulation could contribute to muscle fatigue through reductions in both endplate and t-system excitability.

Changes in t-system ionic homeostasis and membrane potential during AP trains

Skeletal muscle function in vivo generally involves sequential as opposed to lone AP firing. The approach used in this analysis permitted study of ion concentration and membrane potential homeostasis associated with such repetitive firing. It is generally established that repetitive AP firing in skeletal muscle fibers markedly elevates t-system luminal $[K^+]$ (Almers, 1980; Wallinga et al., 1999; Shorten and Soboleva, 2007). It has also been speculated that these could depolarize the t-system membrane sufficiently to produce significant Na^+ channel refractoriness and thereby reduce t-system excitability. Thus, tubular K^+ accumulation has been implicated in muscular fatigue (Sjøgaard, 1990). Experimental studies report such accompanying depolarizations of the resting membrane potential (Freygang et al., 1964).

However, experimental explorations of the possible tubular K^+ changes, depolarization phenomena, the relationship between them, and the extent to which the voltage changes might provide a means for assessing tubular K^+ homeostasis during AP firing are precluded by real-time assessments for $[K^+]_t$ not being available. Nevertheless, CD modeling provided an approach to such an analysis, as it calculates the concentrations of all ions in all compartments. The present studies determined the extent to which depolarization of the resting membrane potential during an AP train in skeletal muscle fibers might result from t-system K^+ accumulation, through comparing experimental recordings with simulations of AP trains using the 20-shell t-system model.

Fig. 7 A shows representative experimental recordings of AP trains with AP-firing frequencies of 6, 15, and 30 Hz in EDL muscle fibers. In each case, the resting membrane potential developed a depolarization over the first ~0.5 s of AP firing that then remained relatively stable despite continuation of the AP trains for 3.5 s. The magnitude of this depolarization increased with the AP-firing frequency. Thus, on average, the maximum baseline depolarization was 0.97 ± 0.15 mV at 6 Hz (n = 13), 2.08 ± 0.12 mV at 15 Hz (n = 23), and 4.4 ± 0.33 mV at 30 Hz (n = 19). On cessation of AP firing, the resting membrane potentials recovered over ~1 s to their prestimulation value. Note that the resting membrane potential during AP firing was recorded immediately before each AP was triggered.

Fig. 7 B shows sarcolemmal potentials during simulated AP trains of the same duration and frequency as in the experimental records depicted in Fig. 7 A. Fig. 7 C then compares the experimental and model records of sarcolemmal depolarization, measured as the difference between the potential immediately before each stimulation and that immediately before the first AP. The CD model successfully replicated the magnitudes of the resting membrane potential depolarizations seen during the experimentally recorded AP trains.

To determine whether the depolarization of the resting membrane potential was associated with alterations in t-system $[K^+]$, Fig. 7 D shows t-system $[K^+]$ for each of the 20 t-system shells during the AP trains. AP firing led to marked elevations in $[K^+]_t$, particularly in the deeper regions of the t-system. At all frequencies, $[K^+]_t$ reached a steady level after ~1 s of AP firing and rapidly recovered after AP firing. The magnitude of change in $[K^+]_t$ increased with frequency. Thus, mean t-system $[K^+]_t$ increased from 5.3 mM before AP firing to ~6.8 mM at 6 Hz, ~8.8 mM at 15 Hz, and ~11.2 mM at 30 Hz.

The cause of t-system $[K^+]$ accumulation was then further explored. First, simulation of fibers without t-system voltage-gated Na^+ channels showed a depolarization of only 0.3 mV when stimulated at 15 Hz for 4 s, in comparison with the 2.1-mV depolarization in modeled fibers with normal t-system ion channel densities. This reflected a much reduced accumulation of K^+ within the t-system (increase of $[K^+]_t$ of around 0.5 mM compared with 5.9 mM under normal conditions). Similarly, there was an absence of resting potential depolarization in a model of detubulation (unpublished data). Therefore, the model suggests that t-system AP firing is responsible for the K^+ accumulation and baseline membrane potential depolarization seen during experimental AP trains, and therefore might be used experimentally to assess whether sarcolemmal APs trigger APs in the t-system.

The simulations demonstrated much smaller sarcolemmal and tubular membrane depolarization than would be expected simply from the alterations in the equilibrium potential of K^+ that the accumulation of K^+ in the t-system would induce. This suggested a role for Cl^- in stabilization of the resting potential during repetitive AP firing.

The role of Cl^- conductance on t-system K^+ homeostasis and the membrane potential during AP trains

Fig. 8 explores the possible role of Cl^- in simulations and experimental measurements of repetitive AP firing using solutions with reduced Cl^- concentration. The replacement of extracellular Cl^- with a monovalent membrane-impermeant anion produced a marked increase in the magnitude of the depolarization observed during repetitive AP firing in both the experimental recordings (Fig. 8, A and B) and the simulations (Fig. 8 C).

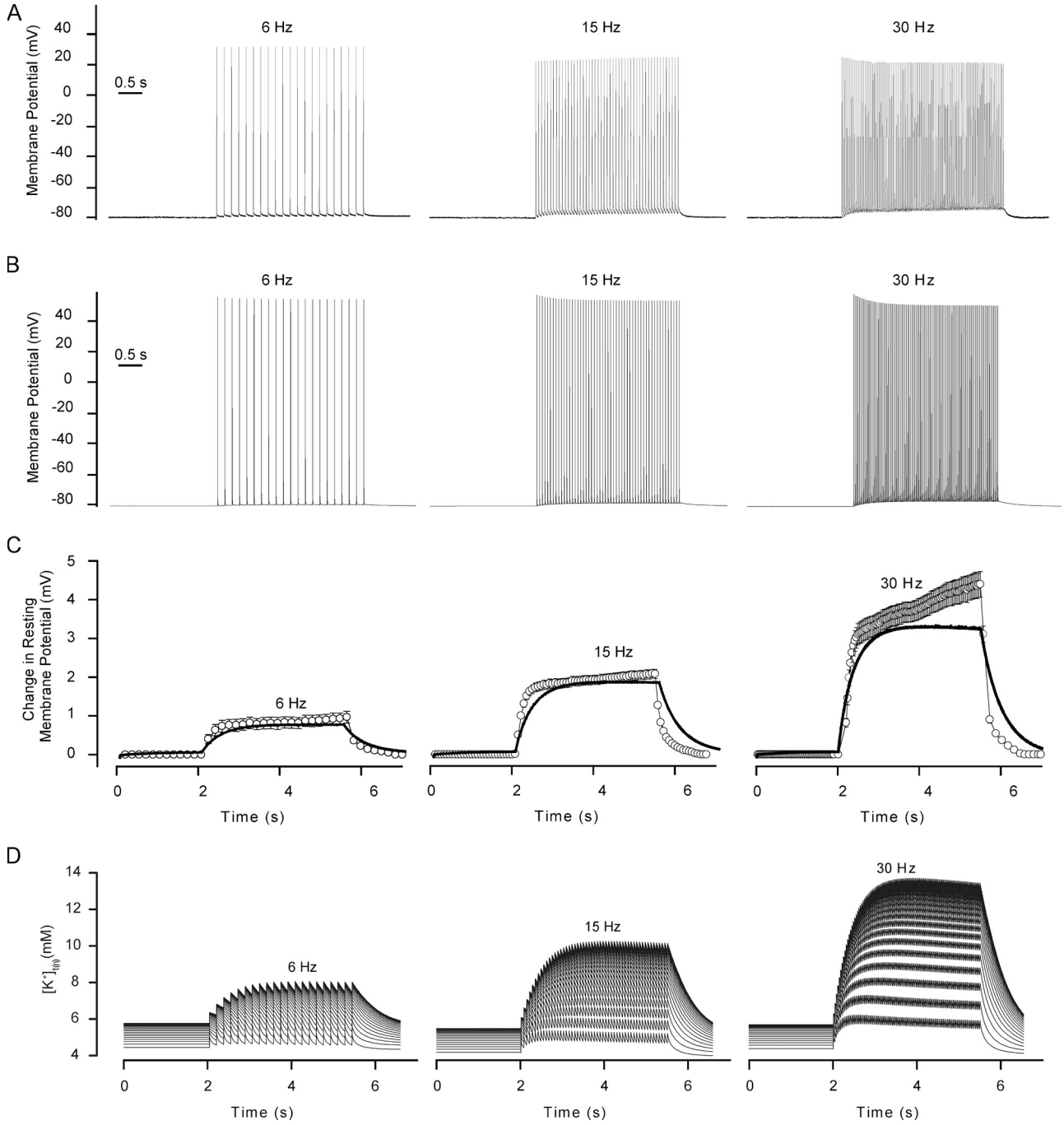

Figure 7. Comparison of AP trains recorded experimentally with those simulated using the CD model. Trains of APs show a similar baseline depolarization of the membrane potential in experimental recordings from rat EDL muscle fibers (A) and in model simulations (B) when stimulated at 6, 15, or 30 Hz. The resting membrane potential during AP trains was evaluated as the membrane potential immediately before injection of excitatory current through the current electrode. At each frequency, the depolarization of resting membrane potential (C) was similar in the experimental (open circles; mean ± SEM) and model records (solid lines). In the model (D), this depolarization resulted from K^+ buildup in the t-system that was greatest in the innermost t-system shell (uppermost traces), and least in the outermost shell (lowest traces).

In previous studies (Pedersen et al., 2009a,b), G_{Cl} was measured in EDL muscle fibers at the different Cl^- concentrations also used in the present study.

Under control conditions G_{Cl} and G_K were 1,314 and 144 μS/cm^2, respectively, giving a G_K/G_{Cl} of 0.11. Reducing extracellular Cl^- to 80 mM increased the depolarization magnitude by around 50% and increased G_K/G_{Cl} to 0.28. Further reduction in Cl^- to 50 mM increased G_K/G_{Cl} to 0.66 and the depolarization by 143%. Entirely withdrawing Cl^- increased the depolarization magnitude by 543%, despite the necessary addition of a small dose of TTX (10^{-8} M) in the solutions to avoid myotonic activity.

These experiments suggest a highly nonlinear relationship of the depolarization during AP firing to G_K/G_{Cl}, in which moderate reductions in G_{Cl}, similar to those during Phase I (G_K/G_{Cl} of around 0.5), only moderately increase the depolarizations, whereas further G_{Cl} reductions markedly increase the depolarizations during AP firing, potentially giving rise to myotonic activity.

Simulations of AP trains with different Cl^- concentrations gave similar findings. Thus, Fig. 8 C shows that for control conditions and for 80 and 50 mM Cl^-, the magnitude of depolarization during the simulated trains closely agreed with the experimental observations. The model further showed that the increased depolarization with reduced Cl^- was associated with minor increases in concentrations of t-system K^+ during the AP trains (Fig. 8 D). In accordance with the experiments in Cl^--free conditions where TTX had to be included to prevent myotonic AP firing, the simulations in the absence of Cl^- resulted in myotonic activity. It was therefore necessary to reduce the maximum permeability of voltage-gated Na^+ channels in the model to perform simulations without Cl^-. Fig. 8 C shows that the depolarization during the simulated AP train in Cl^--free conditions caused a marked rise in the depolarization that, however, was not as marked as in the experimental recordings. In Cl^--free conditions, the rise in t-system K^+ during the AP trains was similar to the rise at 50 mM Cl^-.

G_M regulation during repetitive AP firing has been shown to produce first a decrease in Cl^- conductance (Phase I), and then a large increase in K^+ and Cl^- conductances (Phase II) (Pedersen et al., 2009a,b). The influence of these changes on the magnitude of baseline membrane potential depolarization and t-system ionic homeostasis during repetitive AP firing is demonstrated in Fig. 9. Fig. 9 A shows the first, 40th, and 80th trains of 49 APs at 15 Hz and, on a larger scale, the voltage response to a square test current pulse injected in between the AP trains. This demonstrates an increased voltage response immediately before the 40th AP train, illustrating

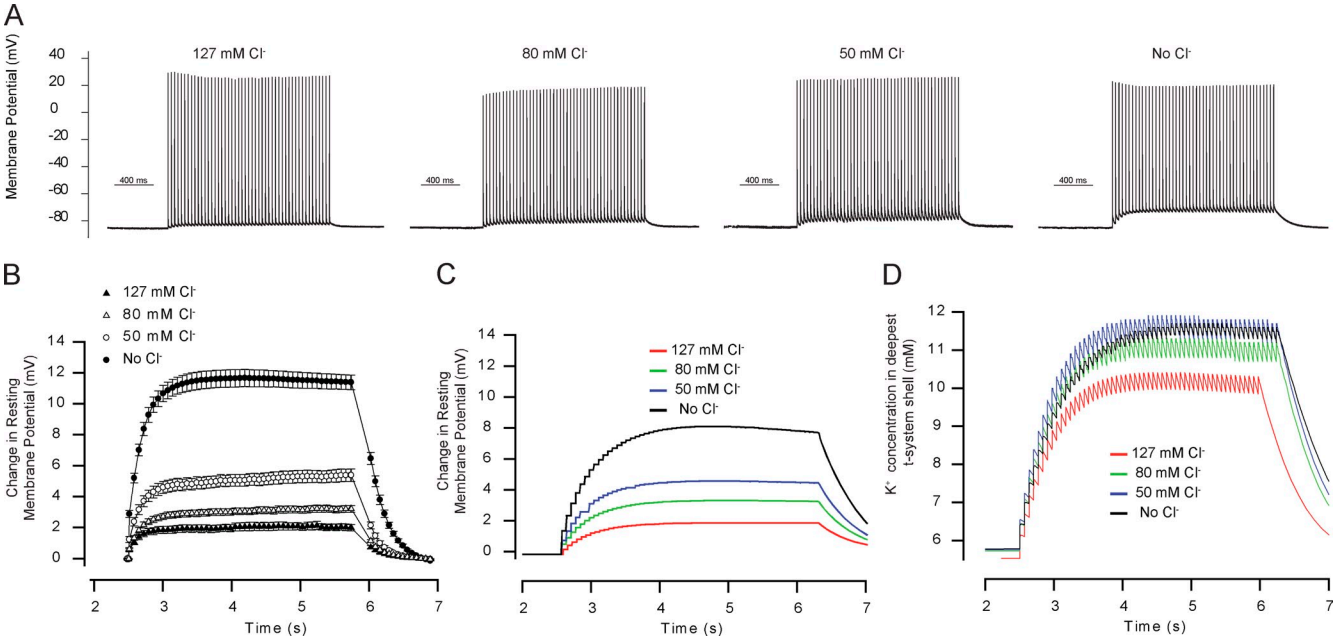

Figure 8. The effect of extracellular Cl^- on the magnitude of the depolarization during AP trains. Two electrodes were inserted into the same muscle fiber, and 3.5-s-long 15-Hz trains of AP trigger pulses were injected. Experiments were conducted using extracellular solutions without Cl^- ($n = 20$) or with different Cl^- concentrations of 127 (control; $n = 11$), 80 ($n = 23$), or 50 mM ($n = 14$). (A) Representative recordings from different fibers at the four Cl^- concentrations. (B) The average change in resting membrane potential during the AP trains at the four Cl^- concentrations. Also presented is the G_{Cl} at the different conditions as reported by Pedersen et al. (2009a) and the resulting G_K/G_{Cl} ratios. (C) The experimental observations of AP trains at the different Cl^- concentrations were simulated, and the change in resting membrane potential was determined. (D) The K^+ concentration in the deepest t-system compartment during the AP trains under the four conditions.

the Phase I G_M decrease, and a decreased voltage response before the 80th AP train, illustrating the Phase II G_M increase. Fig. 9 B demonstrates that the Phase I G_M decrease results in an approximately twofold increase in baseline depolarization, similar to the increase in baseline depolarization seen in low Cl^- solutions (Fig. 8). Yet, a smaller increase in baseline depolarization compared with initial conditions was also recorded during the Phase II increase in G_M.

The precise changes in G_M (Fig. 9 C) and G_K/G_{Cl} ratios (D) were obtained from Pedersen et al. (2009a) to calibrate the model. Thus, Fig. 9 E demonstrates simulations showing a similar pattern of a greatly increased baseline depolarization during Phase I and a smaller increase in baseline depolarization during Phase II G_M changes. However, Fig. 9 F demonstrates that although both Phase I and Phase II increase the baseline depolarization, these G_M changes have opposite influences on t-system K^+ accumulation. Thus, t-system K^+ accumulation was increased in Phase I by ~6 mM compared with 4.5 mM in control conditions, whereas it only was increased by 2 mM in Phase II. In addition, larger excursions in $[K^+]_t$ were seen during each AP in Phase II. Finally, Fig. 9 G shows the influence of membrane Cl^- permeability on baseline depolarization and t-system K^+ accumulation. At low values of P_{Cl}, K^+ accumulation and baseline depolarization are large, as shown in Fig. 8. Between values of P_{Cl} of 10^{-5} cm s^{-1} and 10^{-6} cm s^{-1}, there is a log-linear relationship between P_{Cl} and baseline depolarization, but a smaller influence of P_{Cl} on t-system K^+ accumulation. Thus, in this range that includes the P_{Cl} seen in Phase I, the predominant effect of a decrease in P_{Cl} is to shift the membrane potential closer to E_K. However, an increase in P_{Cl} above normal values, as seen in Phase II, produces a sharp reduction in t-system K^+ accumulation and yet an increase in the magnitude of the baseline depolarization. This latter effect reflects depolarization of E_{Cl} because of an increase in intracellular $[Cl^-]$ as Cl^- currents, rather than K^+ currents, provide the majority of repolarization after each AP. Note that further increases in P_{Cl} prevent t-system excitation.

DISCUSSION

The t-system of skeletal muscle fibers both influences and is influenced by the passage of a sarcolemmal AP. It has a capacitance that is considerably greater than that of the sarcolemma itself (Falk and Fatt, 1964; Gage and Eisenberg, 1969), and therefore its charging could potentially slow the surface conduction velocity. It also possesses voltage-gated ion channels that underlie the t-system AP (Bezanilla et al., 1972; Posterino et al., 2000; Pedersen et al., 2004), which is reflected in recordings of the surface AP as a prominent after-depolarization (Gage and Eisenberg, 1967). Such t-system regenerative electrical activity is thought to result in an accumulation of K^+ in the t-system lumen during repetitive firing of APs (Wallinga et al., 1999; Sejersted and Sjøgaard, 2000).

It has been proposed that such K^+ accumulation could induce loss of muscle excitability through depolarization and consequent inactivation of voltage-gated Na^+ channels, thereby contributing to muscle fatigue (Sejersted and Sjøgaard, 2000). Key to this theory on the etiology of muscle fatigue are observations of elevated extracellular K^+ in plasma (Nordsborg et al., 2008) and in the interstitial space of contracting muscle as obtained using microdialysis probes (Mohr et al., 2004). However, for two reasons such measurements of extracellular K^+ confer very little information on muscle excitability and their membrane potential per se. First, the membrane potential depends heavily on the actions of other ions, their permeabilities, and other transport systems. Second, it has been shown that several mechanisms are activated in the active muscle that can either reduce or enhance the force-depressing actions of activity-induced elevation in extracellular K^+. Thus, muscle activity is associated with elevated Na^+,K^+ pump activity (Overgaard and Nielsen, 2001) and changes in G_M (Pedersen et al., 2009a,b) that might also markedly affect the excitability in working muscle. To deal with the emerging complexity of skeletal muscle excitability, it is desirable to develop mathematical models that will allow multiple parameter changes to be evaluated in combination.

In this study, a model was developed that builds on a realistic t-system geometry as determined using the analytic approach in our companion paper (Pedersen et al., 2011) to evaluate the role of G_M regulation upon excitability and AP conduction velocity in a system with nonlinear voltage- and time-dependent conductances, and to describe and quantify the interrelationships between G_M, t-system ionic homeostasis and the membrane potential during repetitive AP firing.

The new multiple-compartment model was based on the CD model of Fraser and Huang (2004) and Fraser et al. (2005a,b), previously used to investigate ionic and volume homeostasis in amphibian skeletal muscle. The model included background conductances, t-system resistances, and a longitudinal cable structure calibrated to rat skeletal muscle using the analytic model of Pedersen et al. (2011), and voltage- and time-dependent conductances to allow simulation of regenerative AP firing (Wallinga et al., 1999). The ion concentrations within all compartments of the model were shown to possess unique history-independent steady-state values determined by the physical and ion channel parameters of the model. This allowed for the use of the model to predict ion concentrations within the t-system both at rest and during repetitive activity, as well as sarcolemmal and t-system AP conduction.

The model was first used to simulate the passive conduction properties of rat skeletal muscle in the absence of voltage-gated ion channel activity to extend the work

of Pedersen et al. (2011) into a model system with physiological nonlinear background current–voltage relationships. This yielded similar results to those obtained from the model system with linear current–voltage relationships. Thus, the passive conduction velocity of a sinusoidal input current was greater for higher frequency

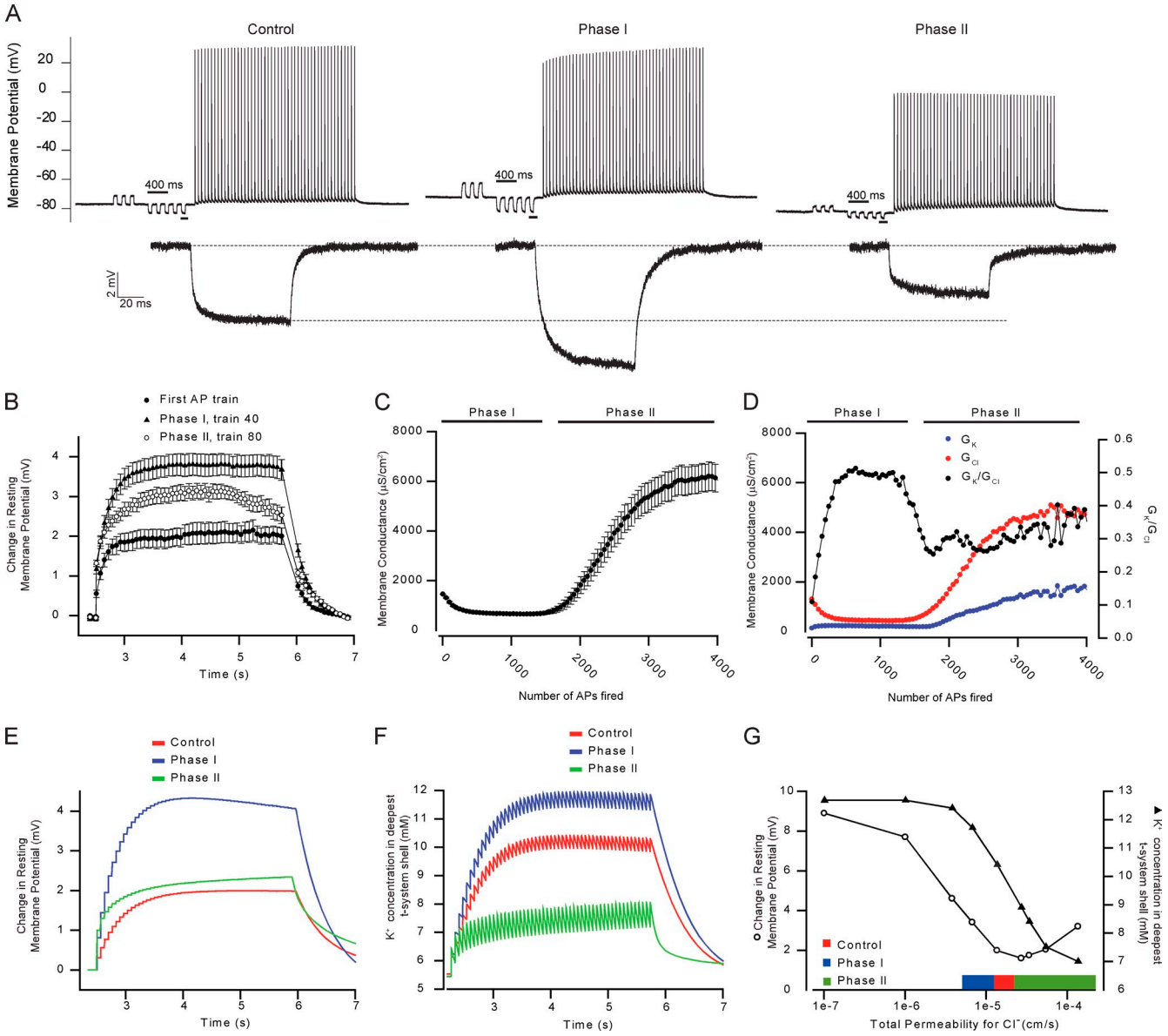

Figure 9. Effects of G_M regulation during Phase I and Phase II on the membrane potential depolarization and t-system K^+ concentration during trains of APs. (A) Representative experimental recordings of the membrane potential from a muscle fibers that was repeatedly activated to fire 49 APs at 15 Hz every 7 s. Recordings show the first (left), the 40th (middle), and the 80th (right) AP train. To highlight the regulation of G_M during AP firing, the membrane potential responses (underlined above) to the small current injections in between the AP trains have been highlighted below. As previously reported (Pedersen et al., 2009a), the onset of AP firing leads to a reduction in G_M, as shown by an enlarged membrane potential deflection during the current injection (Phase I), whereas prolonged AP firing leads to a marked rise in G_M (Phase II), as revealed by a reduced membrane potential deflection. To determine the effect of such G_M regulation in active muscle fiber on the depolarization of the resting membrane potential during the AP trains, the membrane potential before AP firing was subtracted from the potential as recorded 55 ms after every AP. (B) The average change in resting membrane potential during the AP trains during control conditions (first AP train), during Phase I (40th train), and during Phase II (80th train). (C) G_M during AP firing as originally reported by Pedersen et al. (2009a). (D) Changes in the composite conductances for K^+ (G_K) and Cl^- (G_{Cl}) that underlie the changes in G_M in C. (E) The depolarization of the resting membrane potential during the AP trains was determined in simulated AP trains in a similar way that this depolarization was assessed in the experimental recordings in B. (F) The K^+ concentration in the deepest t-system compartment during the simulation of AP trains during the three conditions. (G) The magnitude of depolarization of the resting membrane potential during simulated 15-Hz trains (circles) and the corresponding t-system K^+ in the deepest t-system shell (triangles) for a range of Cl^- membrane permeabilities. Typical values for Cl^- permeabilities for the three conditions have been indicated.

signals, and this frequency–velocity relationship was greatly enhanced by the presence of a significant access resistance (R_A) between the t-system and the extracellular space surrounding the fiber. Furthermore, the presence of additional series resistances within the t-system was shown to steepen this frequency–velocity relationship at higher frequencies (above ~300 Hz).

The study then modeled the influence of active signal regeneration by voltage-gated ion channels upon surface conduction velocity and t-system excitation. This demonstrated that entrance of a propagating AP into a region lacking voltage-gated ion channels produced a sharp deceleration of conduction velocity over distance. Thus, the presence of AP regeneration by voltage-gated ion channels allowed actively propagated APs to show faster peak-to-peak conduction than did passively propagated AP waveforms, even over very short distances (100 µm or less), despite the clear necessity for passive currents to travel ahead of the AP waveform. Fourier transformation demonstrated that high-frequency components of passively conducted AP waveforms declined steeply over distance, thereby accounting for the reduced conduction velocity. In contrast, active regeneration by voltage-gated ion channels was shown to maintain the high-frequency components and thereby maintained a high conduction velocity. Thus, the analysis predicted a log-linear relationship between the maximum total Na^+ permeability ($P_{Na(max)}$) and AP velocity over a range of values of $P_{Na(max)}$ from 0.3 to 10 times the normal physiological value. Fourier analysis then showed that this influence of $P_{Na(max)}$ upon conduction velocity could be attributed to a greater content of high-frequency components in the AP and therefore in the local circuit currents that convey AP propagation.

Fast AP conduction is necessary but not sufficient to achieve synchronous contraction along the entire length of a muscle fiber. There is also a requirement for the surface AP to excite the entire t-system sufficiently to activate dihydropyridine receptors and thereby initiate excitation–contraction coupling (Huang and Peachey, 1989). The present study therefore explored the influence upon t-system excitation of the passage of a sarcolemmal AP for several different t-system models. It demonstrated that a model without a t-system luminal series resistance did not require voltage-gated ion channels within the t-system in order for a surface AP to produce sufficient t-system depolarization (to ~0 mV) for excitation–contraction coupling to occur, despite a physiological R_A. In contrast, a t-system simulated as 20 concentric shells with small physiological resistances between each shell demonstrated a much reduced response (to a peak of only approximately −40 mV in the fiber core) to the passage of a surface AP in the absence of voltage-gated ion channels within the t-system. However, the presence of voltage-gated ion channels within the t-system allowed for the propagation of a full-sized AP through the t-system, producing a peak response of approximately +40 mV in the core of the fiber. The presence or otherwise of voltage-gated Na^+ channels within the t-system had no influence on the conduction velocity of the sarcolemmal AP. Thus, it appears clear that fast AP propagation requires a significant R_A, but a high R_A reduces the passive t-system excitation produced by a surface AP, such that regeneration by voltage-gated ion channels within the t-system is required.

Our companion study (Pedersen et al., 2011) additionally demonstrated that R_A has an important influence on the relationship between G_M and the response of the sarcolemma and the t-system membrane to subthreshold signals. Thus, it predicted that fiber excitation at the neuromuscular junction and t-system excitation are particularly sensitive to regulation of G_M, compared with sarcolemmal propagation. This prediction arose from the property that sarcolemmal AP propagation is conveyed by high-frequency elements in the circuit currents, and the membrane impedance at such frequencies is largely insensitive to G_M. Despite the advantages of the analytical solution in generating the detailed mechanistic insight into the relationship between G_M and excitability, the approach was limited to a linear analysis of subthreshold responses. It was therefore useful to extend the predictions generated in our companion paper using a model system simulating regenerative AP firing.

During repetitive AP firing, there is first an ~60% reduction in G_M (Phase I), and then after prolonged activity, there is a four- to fivefold increase in G_M (Phase II), in comparison to control conditions (Pedersen et al., 2009a,b). The simulations demonstrated that, for 1-ms square current pulses simulating an endplate potential, Phase I produced a minor decrease in the current required to excite an AP, whereas Phase II required a near doubling of this current. This suggests that the sarcolemmal AP excitation is somewhat facilitated by Phase I and markedly reduced during Phase II G_M regulation, even though currents of short duration, comparable to the endplate current, must predominantly flow across the membrane capacitance. Phase II G_M changes were also shown to produce a reduction in the upstroke velocity of the surface AP sufficient to reduce conduction velocity by ~18%, and a reduction in the magnitude of the t-system AP. Additional reduction of $P_{Na(max)}$—simulating activity induced slow inactivation of the voltage-gated Na^+ channel—produced a failure of t-system AP generation during Phase II G_M changes, despite persistence of the surface AP. This functional disconnection between sarcolemma and t-system AP generation illustrates that EMG recordings might miss a failure of excitability under conditions of high G_M and low $P_{Na(max)}$, as might occur after prolonged muscle activity.

Regeneration of the t-system AP by voltage-gated ion channels was shown in the model to take place at the

cost of producing a rapid accumulation of K^+ ions within the t-system during trains of APs. Thus, the K^+ concentration within the deepest parts of the t-system $[K^+]_{t(19)}$ was shown to more than double within 2 s of 30-Hz stimulation. No such K^+ accumulation was seen in fibers lacking voltage-gated Na^+ channels in the t-system, despite the continued presence of voltage-gated K^+ channels. Direct experimental measurement of ion concentrations within the t-system is difficult or even impossible during periods of dynamic change during electrical activity. However, the increased $[K^+]_t$ during repetitive AP firing was shown to produce a stable depolarization of the resting sarcolemmal potential, allowing for comparison of model findings with experimental microelectrode measurements of the membrane potential.

Thus, membrane potential measurements were recorded experimentally from rat EDL muscle fibers exposed to myosin II inhibitor BTS (Macdonald et al., 2005). The experimental results were in close quantitative agreement with the model simulations, with each showing a baseline resting potential depolarization of ~1, 2, and 3 mV during 6-, 15-, and 30-Hz AP trains, respectively, and an associated decrease in maximum AP height. The close quantitative agreement between model and experiments on the depolarization during AP trains permitted the use of the model to investigate the underlying alterations in t-system K^+ homeostasis. This revealed that the dynamics of t-system K^+ accumulation during AP trains and recovery thereafter are very rapid, completing within 1–2 s. This means that measurements of interstitial K^+ using microdialysis probes that offer temporal resolutions in minutes might offer rather little information on the K^+ dynamics in the working muscle (Mohr et al., 2004).

Combining experiments and simulations further demonstrated a significant influence of membrane Cl^- permeability upon t-system K^+ accumulation, membrane potential depolarization, and the relationship between these two variables. Reduction of extracellular $[Cl^-]$ by replacement with an impermeable anion greatly increased the magnitude of the depolarization during AP trains in both simulations and parallel experiments. The G_K/G_{Cl} ratio has been measured previously under identical experimental conditions (Pedersen et al., 2009a). Thus, reductions in $[Cl^-]_e$ increased depolarization in both the model and experimental records by ~50% for 80 mM (G_K/G_{Cl} = 0.28) and >100% for 50 mM (G_K/G_{Cl} = 0.66) when compared with that in solutions of 127 mM (G_K/G_{Cl} = 0.11). Both experimental and model muscle fibers showed myotonic behavior in zero-$[Cl^-]$ solutions; therefore, a small dose of TTX (10^{-8} M) was added in the experiments, and a 50% reduction in $P_{Na(max)}$ was applied to the model. Despite this manipulation, Cl^--free solutions increased the depolarization by 410% in the model and 540% in the experimental studies. This close agreement between the membrane potential records of the model and the experiments prompted detailed analysis of the influence of Cl^- reduction upon t-system K^+ homeostasis using the model. Reduced $[Cl^-]$ was associated with only minor increases in the concentration of t-system K^+ during the AP trains. Thus, under normal conditions, Cl^- influences the resting membrane potential during AP trains by maintaining a high G_{Cl}/G_K, such that the influence of t-system K^+ accumulation on the surface membrane potential is small.

Finally, modeling and experimental membrane potential measurements were used to demonstrate and quantify the influence of the physiological Phase I and Phase II changes in G_{Cl} and G_K upon membrane depolarization and t-system K^+ accumulation that occur during repetitive AP firing. The Phase I reduction in G_{Cl} was shown to approximately double the magnitude of the resting potential depolarization during 15-Hz stimulation in both model and experiment, similar to the influence of reduced extracellular $[Cl^-]$. The model also indicated an increase in t-system K^+ accumulation from ~10 to ~11.5 mM.

The Phase II increase in G_K and G_{Cl} produced a smaller increase in baseline depolarization during 15-Hz AP trains, although the model slightly underestimated the magnitude of the experimentally observed increase. The model showed a large reduction in t-system K^+ accumulation during Phase II, to a peak of ~7.5 mM compared with ~10 mM under control conditions. Thus, during Phase II, depolarization is increased despite a smaller rise in K^+. Indeed, a biphasic relationship was found for the influence of G_{Cl} values on the membrane potential during AP firing, such that both decreases and increases in G_{Cl} in the physiological range increase the resting potential depolarization during AP trains. The effect of a reduction in G_{Cl} was shown to result from a shift of the membrane potential closer to E_K, which is depolarized during activity because of increased $[K^+]_t$. In contrast, an increase in G_{Cl} was shown to produce a large contribution of Cl^- currents to AP repolarization, thereby causing intracellular Cl^- accumulation and hence a depolarization of E_{Cl}. Phase II also increased the rate of recovery to normal values of $[K^+]_t$ after activity. However, the presence of high background ion conductances during AP firing in Phase II produced increases in both inward and outward K^+ movements. Thus, although Phase II G_M changes appear to accelerate reuptake of K^+ from the t-system into the cell and thereby enhance recovery of normal ionic concentrations, they also appear to reduce the energy efficiency of APs by increasing the total ionic fluxes required for each AP.

This study therefore provides a quantitative analysis, supported by experimental results, of the relationships between resting conductances, excitability, and t-system ionic homeostasis in skeletal muscle. It demonstrates that active signal regeneration within the t-system produces K^+ accumulation and quantifies the relationship

between this and the depolarization of the resting membrane potential that is observed during trains of APs. It shows that the Phase I ~60% decrease in G_M during repetitive AP firing enhances endplate and t-system excitability, while also increasing the magnitude of t-system K^+ accumulation and approximately doubling the membrane potential depolarization during AP trains. In contrast, the Phase II increase in G_M decreases endplate and t-system excitability and also enhances K^+ reuptake from the t-system, thereby reducing K^+ accumulation during AP trains. Yet, Phase II also increases the resting potential depolarization during AP trains because of intracellular Cl^- accumulation.

The model that is described here therefore reproduces predictions of electrophysiological behavior and ion concentrations, at rest and during activity, within both the sarcoplasm and the t-system, that are in full agreement with experimental and prior theoretical results. In so doing, it reveals the mechanisms of observed changes including baseline resting potential depolarization during AP trains. Furthermore, it provides a platform for further exploration of electrophysiological activity in skeletal muscle that is applicable where steady-state ion concentrations are not known or expected to undergo significant change. This, in contrast to existing models, permits analysis of the influence of activity-related, genetic, and pharmacological manipulations to the normal physiological state.

J.A. Fraser is supported by a David Phillips Fellowship from the Biotechnology and Biological Sciences Research Council (UK). C.L.-H. Huang acknowledges the support of the British Medical Research Council, the Wellcome Trust, and the British Heart Foundation. T.H. Pedersen acknowledges the support of the Danish Medical Research Council.

Christopher Miller served as editor.

Submitted: 15 February 2011
Accepted: 29 May 2011

REFERENCES

Adrian, R.H., and M.W. Marshall. 1976. Action potentials reconstructed in normal and myotonic muscle fibres. *J. Physiol.* 258:125–143.

Adrian, R.H., and L.D. Peachey. 1973. Reconstruction of the action potential of frog sartorius muscle. *J. Physiol.* 235:103–131.

Almers, W. 1980. Potassium concentration changes in the transverse tubules of vertebrate skeletal muscle. *Fed. Proc.* 39:1527–1532.

Bezanilla, F., C. Caputo, H. Gonzalez-Serratos, and R.A. Venosa. 1972. Sodium dependence of the inward spread of activation in isolated twitch muscle fibres of the frog. *J. Physiol.* 223:507–523.

Cannon, S.C., R.H. Brown Jr., and D.P. Corey. 1993. Theoretical reconstruction of myotonia and paralysis caused by incomplete inactivation of sodium channels. *Biophys. J.* 65:270–288. doi:10.1016/S0006-3495(93)81045-2

Chawla, S., J.N. Skepper, J.A. Fraser, and C.L. Huang. 2002. Osmotic processes in vacuolation and detubulation of skeletal muscle. *Cell Biol. Int.* 26:905–910. doi:10.1006/cbir.2002.0944

Dulhunty, A.F. 1979. Distribution of potassium and chloride permeability over the surface and T-tubule membranes of mammalian skeletal muscle. *J. Membr. Biol.* 45:293–310. doi:10.1007/BF01869290

Dulhunty, A. 1982. Effect of chloride withdrawal on the geometry of the T-tubules in amphibian and mammalian muscle. *J. Membr. Biol.* 67:81–90. doi:10.1007/BF01868650

Falk, G., and P. Fatt. 1964. Linear electrical properties of striated muscle fibres observed with intracellular electrodes. *Proc. R. Soc. Lond. B Biol. Sci.* 160:69–123. doi:10.1098/rspb.1964.0030

Fraser, J.A., and C.L. Huang. 2004. A quantitative analysis of cell volume and resting potential determination and regulation in excitable cells. *J. Physiol.* 559:459–478. doi:10.1113/jphysiol.2004.065706

Fraser, J.A., and C.L. Huang. 2007. Quantitative techniques for steady-state calculation and dynamic integrated modelling of membrane potential and intracellular ion concentrations. *Prog. Biophys. Mol. Biol.* 94:336–372. doi:10.1016/j.pbiomolbio.2006.10.001

Fraser, J.A., C.E. Middlebrook, J.A. Usher-Smith, C.J. Schwiening, and C.L. Huang. 2005a. The effect of intracellular acidification on the relationship between cell volume and membrane potential in amphibian skeletal muscle. *J. Physiol.* 563:745–764. doi:10.1113/jphysiol.2004.079657

Fraser, J.A., C.E. Rang, J.A. Usher-Smith, and C.L. Huang. 2005b. Slow volume transients in amphibian skeletal muscle fibres studied in hypotonic solutions. *J. Physiol.* 564:51–63. doi:10.1113/jphysiol.2004.080911

Freygang, W.H., Jr., D.A. Goldstein, D.C. Hellam, and L.D. Peachey. 1964. The relation between the late after-potential and the size of the transverse tubular system of frog muscle. *J. Gen. Physiol.* 48:235–263. doi:10.1085/jgp.48.2.235

Frigeri, A., G.P. Nicchia, R. Balena, B. Nico, and M. Svelto. 2004. Aquaporins in skeletal muscle: reassessment of the functional role of aquaporin-4. *FASEB J.* 18:905–907.

Gage, P.W., and R.S. Eisenberg. 1967. Action potentials without contraction in frog skeletal muscle fibers with disrupted transverse tubules. *Science.* 158:1702–1703. doi:10.1126/science.158.3809.1702

Gage, P.W., and R.S. Eisenberg. 1969. Capacitance of the surface and transverse tubular membrane of frog sartorius muscle fibers. *J. Gen. Physiol.* 53:265–278. doi:10.1085/jgp.53.3.265

Gallant, E.M., and R.C. Jordan. 1996. Porcine malignant hyperthermia: genotype and contractile threshold of immature muscles. *Muscle Nerve.* 19:68–73. doi:10.1002/(SICI)1097-4598(199601)19:1<68::AID-MUS9>3.0.CO;2-6

Goldman, D.E. 1943. Potential, impedance and rectification in membranes. *J. Gen. Physiol.* 27:37–60. doi:10.1085/jgp.27.1.37

Henneberg, K.A., and F.A. Roberge. 1997. Simulation of propagation along an isolated skeletal muscle fiber in an isotropic volume conductor. *Ann. Biomed. Eng.* 25:15–28. doi:10.1007/BF02738535

Hernandez, J., J. Fischbarg, and L.S. Liebovitch. 1989. Kinetic model of the effects of electrogenic enzymes on the membrane potential. *J. Theor. Biol.* 137:113–125. doi:10.1016/S0022-5193(89)80153-5

Hodgkin, A.L., and A.F. Huxley. 1952. A quantitative description of membrane current and its application to conduction and excitation in nerve. *J. Physiol.* 117:500–544.

Huang, C.L., and L.D. Peachey. 1989. Anatomical distribution of voltage-dependent membrane capacitance in frog skeletal muscle fibers. *J. Gen. Physiol.* 93:565–584. doi:10.1085/jgp.93.3.565

Macdonald, W.A., T.H. Pedersen, T. Clausen, and O.B. Nielsen. 2005. *N*-Benzyl-*p*-toluene sulphonamide allows the recording of trains of intracellular action potentials from nerve-stimulated intact fast-twitch skeletal muscle of the rat. *Exp. Physiol.* 90:815–825. doi:10.1113/expphysiol.2005.031435

Mohr, M., N. Nordsborg, J.J. Nielsen, L.D. Pedersen, C. Fischer, P. Krustrup, and J. Bangsbo. 2004. Potassium kinetics in human muscle interstitium during repeated intense exercise in relation to fatigue. *Pflugers Arch.* 448:452–456. doi:10.1007/s00424-004-1257-6

Nordsborg, N., J. Ovesen, M. Thomassen, M. Zangenberg, C. Jøns, F.M. Iaia, J.J. Nielsen, and J. Bangsbo. 2008. Effect of dexamethasone on skeletal muscle Na+,K+ pump subunit specific expression and K+ homeostasis during exercise in humans. *J. Physiol.* 586:1447–1459. doi:10.1113/jphysiol.2007.143073

Overgaard, K., and O.B. Nielsen. 2001. Activity-induced recovery of excitability in K^+-depressed rat soleus muscle. *Am. J. Physiol. Regul. Integr. Comp. Physiol.* 280:R48–R55.

Pedersen, T.H., O.B. Nielsen, G.D. Lamb, and D.G. Stephenson. 2004. Intracellular acidosis enhances the excitability of working muscle. *Science.* 305:1144–1147. doi:10.1126/science.1101141

Pedersen, T.H., F. de Paoli, and O.B. Nielsen. 2005. Increased excitability of acidified skeletal muscle: role of chloride conductance. *J. Gen. Physiol.* 125:237–246. doi:10.1085/jgp.200409173

Pedersen, T.H., F.V. de Paoli, J.A. Flatman, and O.B. Nielsen. 2009a. Regulation of ClC-1 and K_{ATP} channels in action potential–firing fast-twitch muscle fibers. *J. Gen. Physiol.* 134:309–322. doi:10.1085/jgp.200910290

Pedersen, T.H., W.A. Macdonald, F.V. de Paoli, I.S. Gurung, and O.B. Nielsen. 2009b. Comparison of regulated passive membrane conductance in action potential–firing fast- and slow-twitch muscle. *J. Gen. Physiol.* 134:323–337. doi:10.1085/jgp.200910291

Pedersen, T.H., C.L.-H. Huang, and J.A. Fraser. 2011. An analysis of the relationships between subthreshold electrical properties and excitability in skeletal muscle. *J. Gen. Physiol.* 138:73–93.

Posterino, G.S., G.D. Lamb, and D.G. Stephenson. 2000. Twitch and tetanic force responses and longitudinal propagation of action potentials in skinned skeletal muscle fibres of the rat. *J. Physiol.* 527:131–137. doi:10.1111/j.1469-7793.2000.t01-2-00131.x

Rapoport, S.I., L.D. Peachey, and D.A. Goldstein. 1969. Swelling of the transverse tubular system in frog sartorius. *J. Gen. Physiol.* 54:166–177. doi:10.1085/jgp.54.2.166

Sejersted, O.M., and G. Sjøgaard. 2000. Dynamics and consequences of potassium shifts in skeletal muscle and heart during exercise. *Physiol. Rev.* 80:1411–1481.

Shorten, P.R., and T.K. Soboleva. 2007. Anomalous ion diffusion within skeletal muscle transverse tubule networks. *Theor. Biol. Med. Model.* 4:18. doi:10.1186/1742-4682-4-18

Sjøgaard, G. 1990. Exercise-induced muscle fatigue: the significance of potassium. *Acta Physiol. Scand. Suppl.* 593:1–63.

Wallinga, W., S.L. Meijer, M.J. Alberink, M. Vliek, E.D. Wienk, and D.L. Ypey. 1999. Modelling action potentials and membrane currents of mammalian skeletal muscle fibres in coherence with potassium concentration changes in the T-tubular system. *Eur. Biophys. J.* 28:317–329. doi:10.1007/s002490050214